**Filipa Duque Fragoso de Almeida Carvalho**

Bachelor of Science

# Conception of a Tissue Equivalent Plastic Dosimeter Using Scintillating Fibres for Hadronic Therapy and Space Radiation Effects Studies

Dissertation submitted in partial fulfillment
of the requirements for the degree of

Master of Science in
**Biomedical Engineering**

Adviser: Jorge Sampaio,
Auxiliary Professor, University of Lisbon

Co-adviser: Sofia Pessanha,
Auxiliary Investigator, NOVA University of Lisbon

Examination Committee

Chairperson: Fátima Guerreiro da Silva Campos Raposo
Raporteur: João Gentil Mendes Saraiva
Member: Jorge Miguel de Brito Almeida Sampaio

FACULDADE DE
CIÊNCIAS E TECNOLOGIA
UNIVERSIDADE NOVA DE LISBOA

**September, 2019**

**Conception of a Tissue Equivalent Plastic Dosimeter Using Scintillating Fibres for Hadronic Therapy and Space Radiation Effects Studies**



This document was created using the (pdf)LaTeX processor, based in the "novathesis" template[1], developed at the Dep. Informática of FCT-NOVA [2].
[1] https://github.com/joaomlourenco/novathesis [2] http://www.di.fct.unl.pt

# Acknowledgements

Firstly, I would like to thank my advisers, Jorge Sampaio and Sofia Pessanha, who were always available when I needed and who showed great competence in their work. I also want to thank professor Susana Sério for her availability and friendship. Secondly, I would like to thank FCT-NOVA for its friendly and welcoming environment, if I had the opportunity to go back, I would still pick this school as my second home. I would also like to show my appreciation to LIP, a group of creative and ambitious people who are always eager to involve younger generations in their work, a special thanks to João Gentil, professor Amélia Maio, Rute Pedro, Ricardo Gonçalo and Patrícia Muiño. I would like to thank BEST for taking me into this loving family and provide me with really useful social and technical tools for this new adventure I am about to head in. I will cherish every moment I spent in our organization.

I want to thank my family for going out of their way to give me the best medical support without which I probably could not have made it this far. Thanks for believing in my capabilities and for giving me all the tools necessary to conquer all obstacles. A very warm thought goes to my closest friends who were there for the good and the bad and who, in a way or the other, helped me become a better version of myself. Thank you André, Benny, Borrego, Borralho, Brandão, Cavaleiro, Cruz, Dino, Freire, Guga, Inês Dias, Linda, Pampi, Parada, Pestana, Rocha, Salles, Sérgio, Spínola, Sol, Ticas, Zagalo e Zanal. Finally, I would like to deeply thank my boyfriend, António, who not only is my companion, but also my best friend.

# Abstract

Radiotherapy, and more specifically, proton therapy, presents a state-of-the-art treatment for many types of cancer. Although this relatively new approach to cancer treatment is enticing, it needs to be carefully monitored as it can result in unwanted severe side-effects. The control of the treatment depends on test phases, namely to determine the dose to be deposited at the site, as well as on equipment that monitors the particle beam during treatment, a beam profile monitor, which verifies the stability of the intensity and position of the beam, its range and its straggling effect. This work proposes using scintillating fibres in the assembly of an equipment that allows measurements both for dose determination, as well as for beam monitor profile aplications. Plastic fibres in dosimetry present many advantages such as that gas is not required, the scintillation decay time is typically on the order of a few nanoseconds, the tissue equivalent characteristics of plastic, the spatial granularity is proportional to the fibre diameter and the signal amplitude is proportional to the deposited energy in the fibres. Though this linearity does not happen near the Bragg peak due to quenching, a typical effect in scintillating materials. Another issue is the crosstalk effect between adjacent fibres.

Therefore this work is the beginning of a characterization study to learn about the fibre's properties and evaluate their use in detectors for hadronic therapy and space effects studies. Given the complexity of the problem few results were obtained, nevertheless several iteration of Monte Carlo simulations are performed, we successfully measure the attenuation coefficient of the fibres as we also create a tray in order to quantify the crosstalk effect between adjacent fibres.

**Keywords:** Dosimetry, Scintillating Fibers, Detectors, Radiotherapy

# Resumo

A radioterapia, e mais concretamente, a prototerapia, apresenta-se como um tratamento de tecnologia de ponta para muitos tipos de cancro. Embora esta relativamente nova abordagem ao tratamento oncológico seja atrativa, é necessária uma monotorização atenta, já que poderão ser induzidos efeitos secundários severos. O controle do tratamento depende de fases de teste, nomeadamente para determinar a dose a ser depositada no tumor, assim como de equipamento que monotorize o feixe de partículas durante o tratamento, designadamente um monitor de perfil de feixe, que verifica a estabilidade da intensidade e posição do feixe assim como o seu alcance e a sua dispersão. Este trabalho propõe a utilização de fibras cintilantes na construção de um equipamento que permita medições tanto para a determinação da dose depositada num alvo, assim como para aplicações de monitor de perfil de feixe. As fibras de plástico em dosimetria demonstram ter inúmeras vantagens como, por exemplo, o facto de não ser necessário recorrer-se a um gás, o tempo de decaimento de produção de luz cintilante ser da ordem dos nano segundos, as características equivalentes de tecido do plástico, a granularidade espacial ser proporcional ao diâmetro da fibra e que a amplitude do sinal é proporcional à energia depositada nas fibras. No entanto, isto deixa de ser verdade perto do pico de *Bragg* devido ao *quenching*, um efeito típico em materiais cintilantes. Outro problema que se verifica ainda é o efeito de *crosstalk* entre fibras adjacentes.

Este trabalho é o início de um estudo para caracterizar as propriedades de fibras cintilantes e avaliar o seu uso em detetores para estudos de terapia hadrónica e efeitos de radiação no espaço. Devido à complexidade do problema poucos resultados foram obtidos, no entanto neste trabalho são realizadas várias iterações de simulações de Monte Carlo, é medido com sucesso o coeficiente de atenuação das fibras assim como a criação de um tabuleiro a fim de quantificar o efeito de *crosstalk* entre fibras adjacentes.

**Palavras-chave:** Dosimetria, Fibras Cintilantes, Detectores, Radioterapia

# Contents

# List of Figures

# List of Tables

# Glossary

| | |
|---|---|
| $\delta$-electron | Electrons created during a ionization process with sufficient energy to induce further ionizations. |
| Ionizing Radiation | Ionizing radiation includes any electromagnetic or particle radiation with sufficient energy to ionize common molecules. |
| Phantom | Models used to simulate complex systems, namely, organs of the human body. The most commonly used one is water, but other more complex phantoms can be used to obtain more accurate measurements. |
| Radiotherapy | Radiotherapy is based on the ionizing property of radiation, and acts by killing the tumoral cells and halting their ability to reproduce. |
| Straggling | Dispersion effect due to the media that surrounds the beam or particle. |
| Wall Effect | Distortions in measurements given by the difference in density between the detector boundary. The most common is the delta ray effect, which occurs when multiple delta rays enter the gas from the wall causing the detector to see multiple events rather than a single event. |

# Acronyms

| | |
|---|---|
| CSDA | Continuous Slowing Down Approximation. |
| GCR | Galactic Cosmic Rays. |
| LET | Linear Transfer of Energy. |
| LINAC | Linear Accelerator. |
| MOSFET | Metal Oxide Semiconductor Field Effect Transistor. |
| PMMA | Polymethyl Methacrylate. |
| PMT | Photomultiplier Tube. |
| POM | Polyoxymethylene. |
| PS | Polystyrene. |
| PSD | Plastic Scintillating Dosimeters. |
| PT | Proton Therapy. |
| RBE | Relative Biological Effectiveness. |
| RT | Radiotherapy. |
| SFOD | Scintillating Fiber–Optic Dosimeter. |
| SiPM | Silicon Photomultipliers. |
| SOBP | Spread Out Bragg Peak. |
| SOI | Silicon on Insulator. |
| SV | Sensitive Volume. |
| TEPC | Tissue Equivalent Proportional Counter. |
| TEPS | Tissue Equivalent Plastic Scintillator. |

Chapter 1

# Introduction

## 1.1 Context

Dosimetry is an area of great interest given its range of applications in radiation dosimetry, radiation protection and radiation medicine, both in diagnostic and radiotherapy (RT). Radiation dosimetry is the measurement, calculation and assessment of the ionizing radiation dose absorbed by matter [1], where dose is a quantity that quantifies the energy absorbed by matter. Dosimeters are the apparatus conceived to measure the absorbed dose. We could say this is the main field of Dosimetry, as radiation protection and radiation medicine are supported by radiation dosimetry developments.

As far as radiation protection goes, this area focuses on the assessment of radiation effects in living tissues and material components. The risk from carcinogenesis is the major concern, although mutations, and birth defects are also a concern. To ensure the safety of workers exposed to radiation on a daily basis and that of patients exposed to radiation, certain requirements should be met, namely the dose accuracy. For radiation workers or patients subjected to exams with low ionizing radiation, 50% for dose accuracy is widely accepted. In medical applications, such as RT, the accuracy should be greater than 5% [2]. Another important consideration is that there are certain tissues with higher sensitivity to radiation. For instance, the blood-forming cells in the bone marrow are most sensitive for the induction of leukemia [2]. A crucial study point in radiation protection is the shielding from dangerous radiations as well as material degradation over time.

In what concerns radiation medicine, dosimetry gives a quantitative correlation between the radiation that is delivered and the respective biological response [3]. Inside radiation medicine we have treatment planning, medical imaging and treatment [3]. The applications in treatment planning include understanding what kind of treatment is most

appropriate given the type of tumor, its location and size, and by understanding the exposure of healthy tissues to radiation. In fact, today there are companies whose sole purpose is to optimize treatments mostly via through the development of software that simulates different types of treatment. Dosimetry during treatment is used to achieve and control the efficacy of therapeutic treatments [3]. It is estimated that about two-third of all cancer patients will be subjected to some form of RT [4].

## 1.2 Historical Perspective

The biological consequences of ionizing radiation were not recognized until X-rays were first man produced [2] in 1895 by Wilhelm Conrad Röntgen [4, 5] when he took the first X-ray image of his wife's hand [5]. In the years that followed, several studies were conducted reporting the use of X-rays and radium in medicine [4]. However, very little was understood regarding the mechanisms inherent to the interaction between radiation and biological tissues.

An important mark in the radiological community was achieved in 1928 when the International Commission on Radiological Protection (ICRP) was founded to address the question of radiation protection [4]. From 1930 to 1950 there was a significant scientifical progress in radiotherapy. Brachytherapy was first introduced along with electron and proton beam therapy [4, 6]. In the beginning of the 1950s, intense cobalt-60 sources were widely used in external beam RT (teletherapy) machines, which produced a beam of gamma rays directed into the patient [7]. In the 1970s, these started to be replaced by medical linear accelerators (LINACs), which can produce a high energy electron beams or X-rays. Nowadays, most developed countries have abandoned the use of cobalt units and RT is done with LINACs.

The 1970s and 1980s were characterized by the introduction of proton therapy (PT). Even if their first clinical use dates back to 1954, it was only on the late seventies that proton beams were successfully applied to treat cancer [4]. Today there are over 75 particle therapy centers worldwide (including proton and carbon beams) and the number is increasing rapidly as PT is now a commercial off-the-shelf technology.

Some of the most important of these scientific developments has been the paradigm of fractionated dose delivery, where the treatment is done in several sessions of small doses (∼2 Gy) adding up to the desired dose and the of Intensity-Modulated Radiotherapy, where treatment is done with beams in multiple directions in the tumor volume. This only became possible due to the technological advances in X-ray production and delivery, the improvements in imaging and computer-based treatment planning and the development of models that predict how cancers behave and how they should be approached therapeutically [4].

Figure 1.1 compares dose in depth deposition for different particles and energies. The dose profile for photons is characterized by a rapid rise at superficial tissue layers (build-up region), followed by an exponential decay. This means that in-depth photon treatment

of tumors necessarily implies an overdose before and after the volume to be irradiated. However, in the last decade new techniques have been developed to significantly reduce overdose in photon treatment.

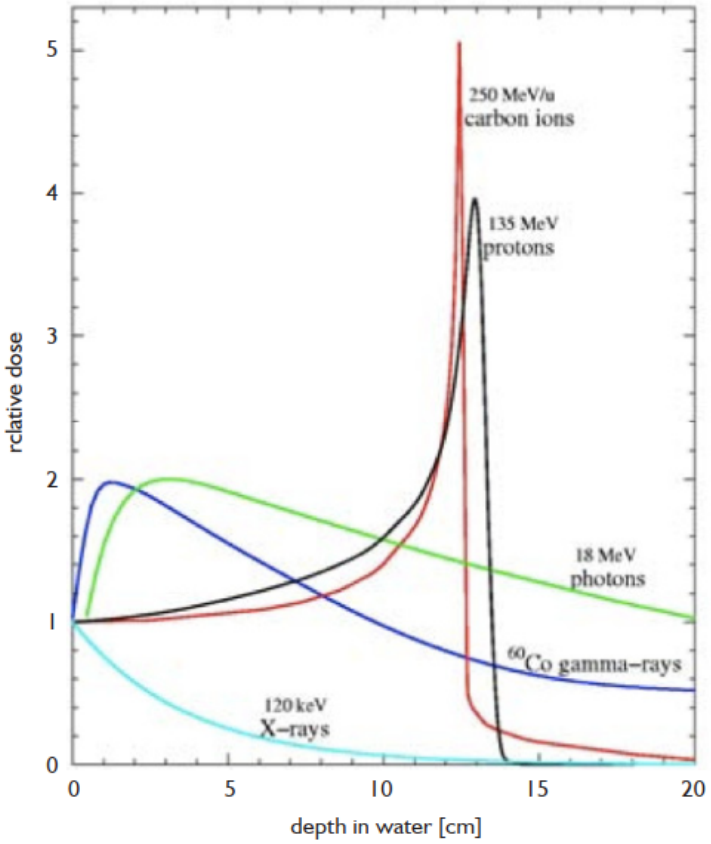


Figure 1.1: Depth dose for different particles and for different energies in water [7].

From a dosimetric point of view, the main advantage of using protons instead of photons in radiotherapy is shown in figure 1.1. The dose for massive charged particles is characterized by a growth in depth, ending at a very pronounced maximum, called the Bragg peak. By varying the beam energy, it is possible to position the Bragg peak at various depths and thus conform the highest dose to the tumor volume. However, since particle interactions with the medium are statistical, the energy lost and the number of collisions required to bring protons to rest varies slightly (i.e., some protons lose less energy and travel further than others). Hence, there will be a small variation in the range, known as straggling, which means that Bragg's peak position has an associated uncertainty [8].

## 1.3 Motivation

The precise determination of proton range is currently a major challenge in PT, as a small variation in range means very high overdose beyond the tumor's distal edge. The

main objective of this work is to study the possibility of developing a system based on scintillation optical fibres that allows dosimetry with sub-mm resolution. To this end, we studied:

- Physical and optical properties of scintillating optical fibres;
- Simulate irradiation scenarios to study the behaviour of the optical fibres in PT dosimetry;
- Study different coating methods and materials to maximize light trapping efficiency;
- The design of a tray to quantify crosstalk effects between adjacent fibres.

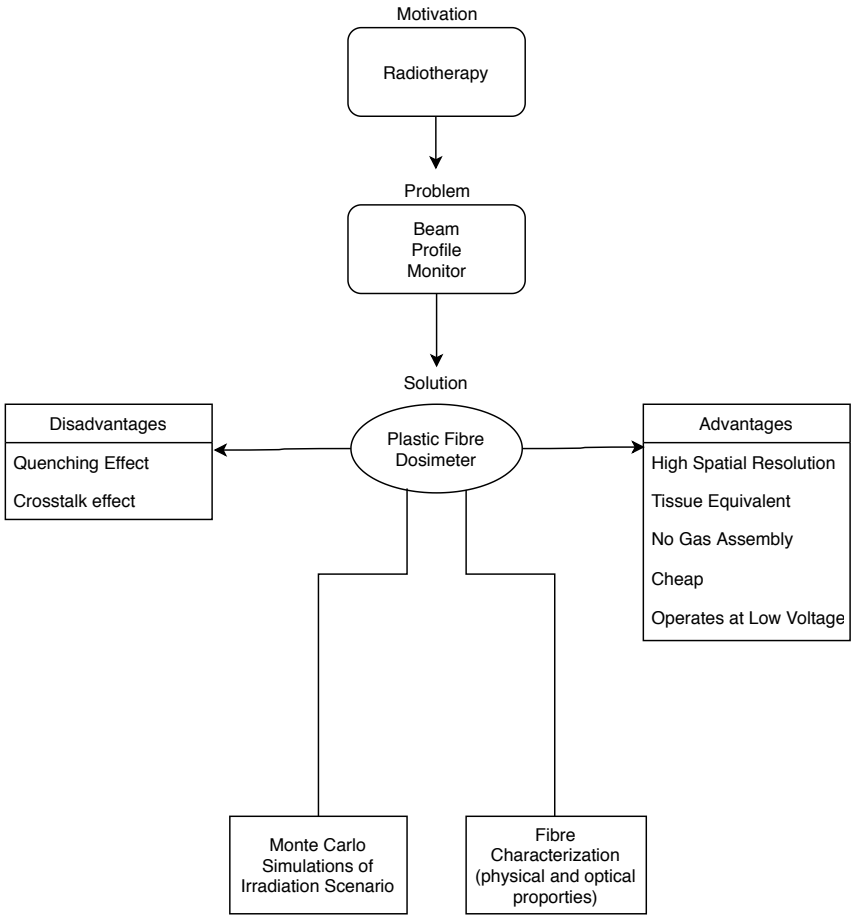


Figure 1.2: Diagram highlighting the advantages, disadvantages and methods for the solution of a plastic fibre dosimeter for the beam profile monitor problem in radiotherapy.

## 1.4 Thesis Outline

In the next chapter, there is a brief description of the dosimetric quantities, concepts and their relation to biological systems. The average concepts of dose and linear energy

transfer do not describe accurately the stochastic effects of energy deposition at the microscopic scale. For this reason, we also introduce the relevant microdosimetric quantities that should be measured at this scale.

Further on, we describe the state-of-the-art microdosimeters. In particular, we describe recent progresses made by a group in Heidelberg that is developing a PT tracking system similar to the dosimeter we want to develop. The chapter ends with a short overview of the physical properties that characterize the scintillating fibres.

Chapter 3 explains the methods materials used in this work and in Chapter 4 the results are presented. Future work and summary of the document is discussed in Chapter 5.

Chapter 2

# Background

## 2.1 Dosimetric Quantities

### 2.1.1 Absorbed Dose

Dose ($D$) is the mean value of the imparted energy absorbed per unit mass at a point in a body and comes in units of J/kg or Gy (Gray). Since dose is a non-stochastic quantity, it can be defined as a point function in differential form [8]:

$$D = \frac{d\bar{\varepsilon}}{dm} \tag{2.1}$$

Where $d\bar{\varepsilon}$ is the mean energy imparted in a volume of mass $dm$. Taking in account the time exposition to a given type of radiation an absorbed dose rate, $\dot{D}$, is defined as,

$$\dot{D} = \frac{dD}{dt} = \frac{d^2\bar{\varepsilon}}{dmdt} \tag{2.2}$$

### 2.1.2 Linear Energy Transfer

Linear Energy Transfer, LET, as defined by the International Commission on Radiation Units (ICRU), is a measure of the loss of energy due to electronic collisions per unit distance along the path of a charged particle (incident or secondary). The unrestricted LET (that includes the energy lost to high-energy $\delta$-electrons) is identical to the electronic stopping power:

$$LET = -\left(\frac{dE}{dx}\right)_e \tag{2.3}$$

LET can be classified as being high or low. High LET (which ranges between 20 to 100 keV/$\mu$m) is usually produced by protons, alpha particles, and heavy ions [9], as they have

large masses and thus, the collision probability (cross section) is high. Therefore, these particles will be more easily stopped and will transfer a lot more energy on impact. Low LET particles (< 10 keV/$\mu$m) are, for example, beta and gamma radiation. Beta radiation is low LET because when compared to protons, the electrons have much smaller mass, thus resulting in a greater distance between ionizing collisions and a lower energy transfer. However in some cases, like low energy Auger emission, electrons can be considered high LET radiation because they have a very small range, rendering a high energy deposition per unit length [10]. In figure 2.1 it is possible to observe what was stated above regarding the difference in the travel distance between high and low LET radiation.

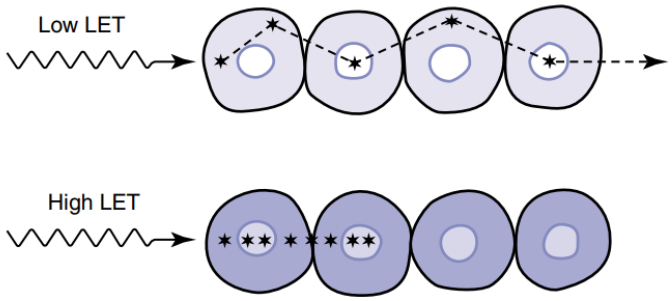


Figure 2.1: Representation of the comparative effects of low and high LET radiations in a population of cells [9].

## 2.2 Microdosimetric Quantities

It is through microdosimetry that we are able to study the impact of radiation at the micron scale. This has special interest to study the effect of radiation in cellular systems. This type of studies proves to be fundamental for radiation protection, as it helps to determine the probability of injury or lethality on living cells during radiotherapy [8, 11].

Rossi *et al.* were the very first recognizing that there is a fundamental difference between macroscopic dose and the energy deposition in microscopic structures [12]. Since ionizing radiations interact in a discontinuous way with matter, dose and dose rate are statistical averages that disregard the inherent random behaviour of stochastic processes. Because of that, the knowledge of absorbed dose gives little information about the energy deposited in cellular and sub cellular structures. As we increase the resolution, the fluctuations are more and more substantial, for both dose and for more densely ionizing radiations [12].

### 2.2.1 Specific Energy

Specific energy is the analogous to the absorbed dose in dosimetry and it comes in units of J/kg, or Gy. It is defined as quotient of $\varepsilon$ by the volume mass $m$, where $\varepsilon$ is the energy imparted by ionizing radiation in a single interaction,

$$z = \frac{\varepsilon}{m} \tag{2.4}$$

Specific energy is a hard to compute quantity given that it is almost impractical to carry out the microscopic track structure simulation because of the computational-time limitation [13].

### 2.2.2 Lineal Energy

This quantity is the analog to the stochastic version of LET, and by definition it only takes into account the energy deposited by a single event. Lineal energy is commonly presented in units of keV/$\mu$m and is defined as the quotient of $\varepsilon$ by $\bar{l}$, where $\varepsilon$ is the energy imparted to matter in a volume by a single energy deposition event, and $\bar{l}$ is the mean chord length in that volume [8, 14].

$$y = \frac{\varepsilon}{\bar{l}} \tag{2.5}$$

The mean chord length in a convex volume is:

$$\bar{l} = \frac{4V}{S} \tag{2.6}$$

where $V$ is the volume and $S$ is the surface area of the target body.

The probability distribution of lineal energy (f (y)) and dose distribution (d(y)) are fundamental functions in microdosimetry. The relationship between $f(y)$ and $d(y)$ is:

$$d(y) = \frac{y f(y)}{\bar{y}_F} \tag{2.7}$$

From this relationship we can see that higher lineal energies deposit a higher dose [14]. $\bar{y}_F$ and $\bar{y}_D$ have the following averages defined as

$$\bar{y}_F = \int_0^\infty y f(y) dy \tag{2.8}$$

and

$$\bar{y}_D = \int_0^\infty y d(y) dy \tag{2.9}$$

In which $\bar{y}_F$ is the frequency mean lineal energy, and $\bar{y}_D$ is the dose mean lineal energy. The spectrum is traditionally displayed as a log–linear plot due to the wide range of lineal energy (from 0.01 to 103 keV/$\mu$m) [14]. One of the aims of this project is to design a system able to measure the d(y) and f(y) distributions.

## 2.3 Survival Curves

In the early study of radiotherapy, it was observed that the same dose of different radiation produced different biologic responses in the same tissue, as it's possible to observe in figure 2.2. The survival curves depicts the relationship between the fraction of cells retaining their reproductive integrity and the absorbed dose of radiation. These are usually plotted on a logarithmic scale [8, 14]. There are several factors that determine the behaviour of survival curves such as the radiation dose, number of dose fractions, this means giving smaller doses over a longer period of time, and the type of cells that are being irradiated, as well as the mitotic phase they are in [15–17]. Figure 2.2 shows the survival curves for different kind of particles and energies.

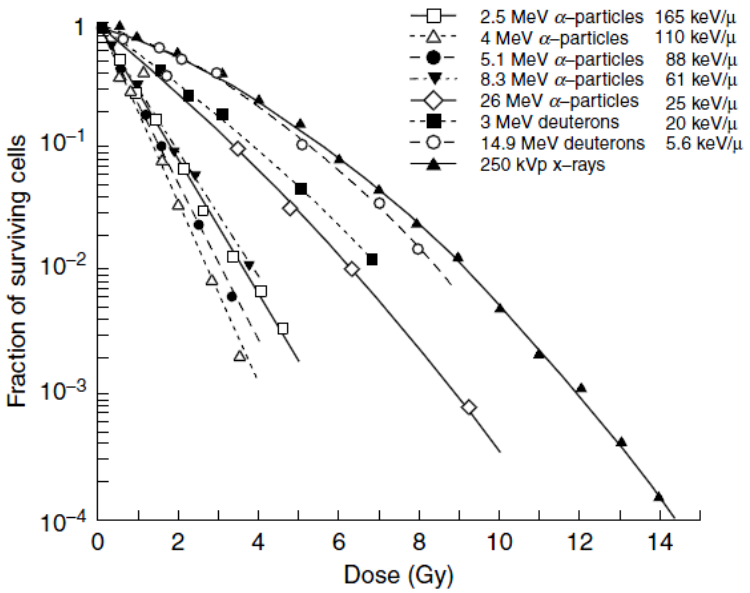


Figure 2.2: Cell survival curves as a function of the dose for different kind of particles and energies [18].

Several mathematical models were developed to describe the experimental data of the survival curves. High-LET radiation, like alpha-particles, produce a exponential decay of the survival fraction [19]. The most simple model is inactivation by single event, represented by a Poisson distribution [8, 20]:

$$S(D) = e^{-\alpha D} \tag{2.10}$$

Where $S$ is the surviving fraction when the mean number of lethal events in cells caused per unit absorbed dose, $D$, is equal to $\alpha$ [8].

Low-LET radiation like X-ray exhibit a 'shoulder' at low doses before the onset of the exponential decay. In this case, the most frequently used model to fit the data is the linear quadratic (LQ). This model only accounts for the damage imparted to the DNA molecule,

especially the double stranded breaks, which are highly likely to induce death. We can consider two types of damage [8, 19]:

- Type A: the ionizing particle breaks the two strands of DNA (double strand break) with only one collision.
- Type B: two different particles break each strand of DNA at close sites, and considering that there was not enough time for the cell to recover from the first collision.

$$S(D) = e^{-\alpha D - \beta D^2} \tag{2.11}$$

Where $\alpha$ is the constant that represents the probability of lethal damage due to damage of type A, and $\beta$ the constant that represents the probability of lethal damage by type B damage [19, 21]. Within this interpretation, high-LET radiation produces only type A damages, since $\beta = 0$. Because LQ model needs only 2 [19, 21] parameters to compute, it is easier to fit several different types of survival curves [20].

## 2.4 Relative Biological Effectiveness

The survival curves show that equal doses of different LET radiations do not produce the same biologic response [9]. This phenomenon is quantified by the Relative Biological Effectiveness (RBE), defined by,

$$RBE = \left( \frac{\text{Dose from 250 keV X-ray}}{\text{Dose from test radiation}} \right)_{\text{same endpoint}} \tag{2.12}$$

Historically, the biological effectiveness of the beam is determined by the comparison with a 250 keV X-ray beam that was the primary radiation beam available in the early days of radiotherapy [9]. Depending on the study it is possible that another beam is used as a reference to determine the RBE. In order to obtain the values to compute the RBE using equation 2.12, it is necessary to irradiate cells and plot the survival curves, as a function of dose and compute RBE for the same endpoint. The endpoint could be, for instance, the dose at which half of the cells died.

The determination of RBE is a crucial step in clinical proton and heavy ions radiotherapy. Given the type of treatment, the RBE factor chosen depends mostly on the type of radiation to be used [22, 23]. There have been several studies where it was observed that irradiating different types of cells with the same radiological source, refuted the assumption that all the same type of radiations cause the same biological effect [22]. Most of the studies that study the RBE-LET relationship focus on the damage inflicted to DNA [21, 24, 25] where it is unanimous the conclusion that there is a relationship in the induction of mutations with the type of LET. In one of these studies, it was observed that RBE values for induction of double strand breaks generally increase slightly with the LET (by a factor 2-3). This implies that at least part of the processes involved in the conversion of DNA

lesions to cellular effects could be dependent on LET [21]. Recent studies also suggest that the DNA damage induced by high-LET radiation is qualitatively different from that induced by low-LET radiations [24].

But there are some serious limitations in using this concept solely to explain biological effectiveness of radiation and the differences between types of radiation. It has been shown that there are two other major physical factors which can influence the survivability of mammal cells: distribution of the dose in time (fractional dose irradiation) and the spatial distribution of energy deposition along the tracks of ionizing particles [4, 21]. Firstly, LET alone does not take into consideration variations in the track structure pattern of different ion species. For example, ions with high energy and high atomic number (HZE) produce considerably more $\delta$-electrons than low energy and low atomic number ions (LZE) for the same LET [13, 14]. Secondly LET does not assume variation through the site of interest [14, 26]. Finally, LET is a non-stochastic average quantity which means it does not account for the random fluctuations in energy deposition and range straggling [14].

## 2.5 Radiotherapy Principles

Radiotherapy is a type of cancer treatment that uses high doses of radiation to either disable the reproductive capability of cancer cells, or to kill them by permanently damaging the cells' DNA [27]. This is achieved by ionization, the most important form of radiation interaction in RT [20].

There are two main types of radiotherapy, external beam and internal. Throughout this thesis we will mainly focus on external beam therapy.

### 2.5.1 External Beam Therapy

In this section only proton and ion beam therapy will be addressed, although electron and photon beam therapy are commonly used.

Proton and ion beam therapy are medical treatments built around an intrinsic property of these charged particles that has to do with the way they deposit their energy in matter. By plotting the energy deposition with depth, it is possible to identify a peak for which energy deposition has a maximum, the Bragg peak. The depth at which this peak occurs has to do with the initial energy of the particle and with the material the particle is traveling in. The particle range, $R$, measures the average distance the particles travel before stopping and deposit most of their energy. Range comes usually in units of $g/cm^2$. By dividing the range by the density of the media, you get the average distance the particles travel before stopping and deposit most of their energy. NIST (National Institute of Standards and Technology) has available on their website a dataset with ranges of particles in function of their initial energy for several different materials [28, 29].

There are several techniques in external beam therapy used to scan all of the tumor volume with high accuracy in depth. For instance, you can create a spread out Bragg peak (SOBP) by varying the range and the fluence of the beam [6]. By combining multiple Bragg curves of particles with different ranges, the sum of those curves adds up to a plateau of high energy at a certain interval of depth. Figure 2.3 illustrates the rational that was just explained.

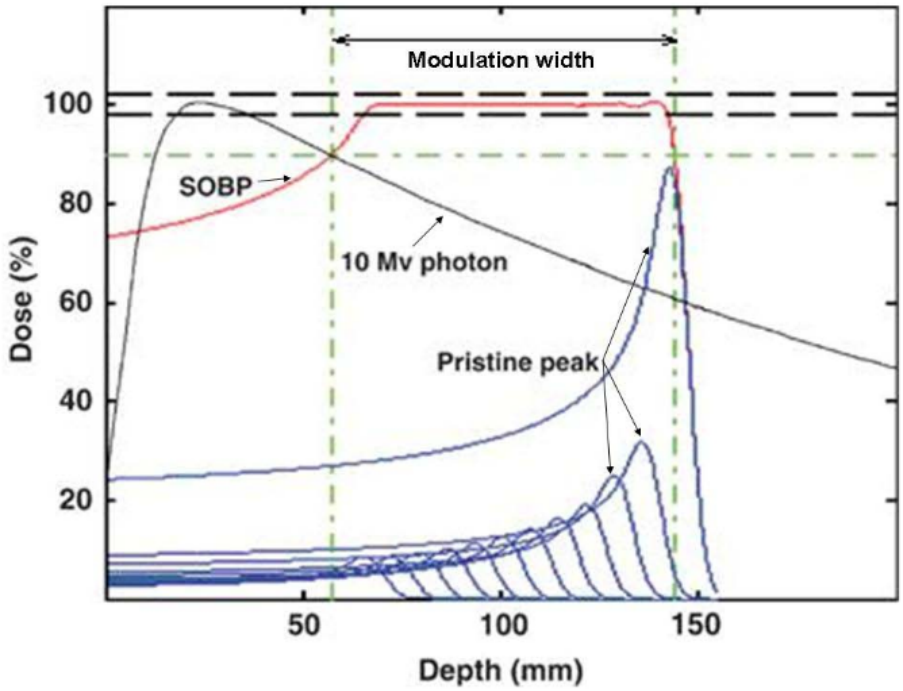


Figure 2.3: Dose plotted over depth for an ion beam with different energies. A Spread out Bragg peak is created by having particles with varying range hitting our target. The integration of ions with different Bragg peak creates a plateau of maximum energy deposited [6].

SOBP can be created by varying the energy of the beam. Range modulation can be achieved by 3 different ways: variable reach shifter [11], rotating modulator wheel [20] and weight optimization [30]. The most common method is to use the rotating modulator wheel. This wheel has angular segments of widths and thicknesses corresponding to the pullback and weight of individual Bragg peaks that comprise an SOBP (figure-2.4a) [20].

Another treatment technique is to create an aperture-compensator system which shapes the fields to a desired target profile using patient customized molds (figure 2.4b). They are often made out of Brass since it offers the best choice in terms of cost, weight and production of secondary radiation [31].

Because protons can be deflected magnetically, another alternative is to generate a narrow mono-energetic "pencil" beam and control it magnetically across the target volume. The depth scan is done by means of energy variation and it works as follows: One starts with the deepest layer, corresponding to the highest energy, and scans the plane.

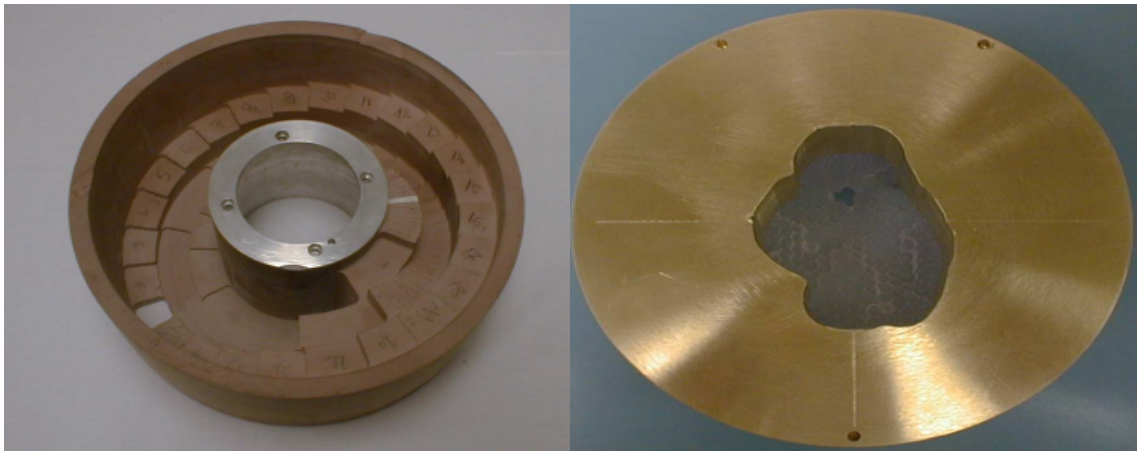

(a) Photograph of a range shifter.

(b) Photograph of the aperture-compensator system.

Figure 2.4: Set of picture of elements that may take part in radiotherapy treatment [31].

The energy is then reduced and so forth until all 20-30 layers have been delivered.

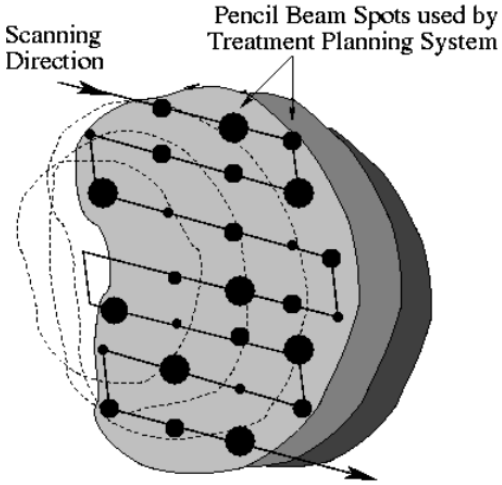


Figure 2.5: Schematic representation of pencil beam treatment. The intensity can be varied from spot to spot, or continuously along the path [31].

## 2.6 Radiation in Space

In space there are two main sources of radiation: the galactic cosmic rays (GCR) and the solar wind [32]. Additionally, solar particles are trapped in the Earth's magnetic field producing the radiation belts around our planet known as the Van Allen belts. The interaction of the GCR with the upper atmosphere also produces showers of secondary radiation that reaches the ground. Space radiation and induced radiation in the atmosphere places not only astronauts but aviation crews as well at significant radiological risk. Not only is necessary to guarantee the safety of the astronauts and aviation crews,

but it is also imperative to shield the electronics from radiation [33].

The main problem of space radiation is that unlike most of the natural and artificial radiation on the ground, which is constituted by photons and other low LET particles, the GCR and solar wind is made of high LET ions. The RBE of most of these ions is not well known and studying their biological effects is an important line of research nowadays [34]. Also the microstructure of the energy deposition of the space radiation fields is an important issue in radiobiological studies with these ions. For these reasons there are several missions that include detectors to measure microdosimetric distributions. For example, the TEPC Environmental Monitor model was commissioned by NASA and used on the Mir Space Station, the Space Shuttle Discovery and other NASA spacecraft, and airplanes [35]. Currently there are mini-TEPC being tested in airplanes.

These are also possible future applications of the system we started to study in this work. However, this analysis was not developed in this thesis.

## 2.7 State-of-the-Art Microdosimeters

This section will cover the most commonly used detectors for dosimetry and microdosimetry and evaluate their advantages and disadvantages.

An ideal radiation detector should mimic as closely as possible the medium in which the absorbed dose will be measured. The charged particles crossing a detector will then interact in a manner similar to that within the medium [36]. Water and plastic are often the dose-absorbing medium of choice for phantoms used in dosimetry because for their similar composition to tissue. That is why for biological assessment the detectors are tissue equivalent.

There are certain characteristics that should be considered when creating a detector.

- Stability - Stability is the capability of the detector to reproduce the results with as little variation as possible [1, 36]. The longer the detector is able to preserve this capacity, the more stable it is. Radiation damage is an important aspect to consider for the stability of a dosimeter, especially when using plastic scintillators, as they quickly degrade with high-energy radiation and this can influence their ability to produce or transmit light, resulting in an overall loss of scintillating efficiency [36].

- Precision and Accuracy - Precision can be estimated from the data obtained in repeated measurements and the overall precision is reflected on the standard deviation of the results. The accuracy of dosimeter measurements expresses the proximity of their expectation value to the true value of the quantity being measured.

- Dose rate proportionality - Ideally, the detector should be independent of the dose rate as well as the overall dose. A constant dose sensitivity throughout the range provides a linear response that is desirable for ease of calibration and interpretation [36].

- Resolution - Depending on the purpose of the detector. Sometimes the objective is to accurately measure dose distributions, but there also could be the case where the goal is just to assess the overall macroscopic dose absorption.
- Temperature - Temperature dependence should always be considered, especially for detectors used for *in vivo* dosimetry.
- Pressure - Pressure dependency is relevant for detectors that rely on gaseous supply, for instance, ion chambers.

The value output given by a microdosimeter is calculated based on several corrections factors. For instance, Tissue Equivalent Porportional Counters (TEPC) need to consider wall effects, as well as volume recombination, which occurs when ions and electrons recombine on their way to the electrodes [1], and Tissue Equivalent Plastic Scintillators (TEPS) generally suffer a degradation over time [36, 37] as mentioned previously as well as having a quenching effect associated.

### 2.7.1 Tissue Equivalent Plastic Scintillators

This type of detectors use materials that scintillate when radiation interacts with them. They are generally comprised of three main components: a detector probe, a light guide, and a photodetector [38], generally a photomultiplier (PMT). This is the kind of detector we aim to build during this work, where the scintillating material are the optical fibres.

Some of the advantages of using plastic scintillators as detectors for dosimetry are the intrinsic water equivalence properties of plastic polymers [39]. Furthermore, these detectors have been shown to accurately determining the absorbed dose and the dose distribution in a comparative study of small volume dosimeters [38]. In Table 2.1 it is possible to see different physical parameters for polysterene, a material that is commonly used in scintillators. It is also the material of the core of the fibres used in this work.

Table 2.1: Physical parameters for polystyrene and water [36].

| Parameters | Polysterene | Water |
|---|---|---|
| Density (g/cm$^3$) | 1.06 | 1.00 |
| Ratio of number of e- in the compound to molecular weight (Z/A) | 0.5377 | 0.5551 |
| Electron density ($10^{23}$e-/g) | 3.238 | 3.343 |

The Heidelberg Ionenstrahl Therapiezentrum (HIT) is developing a prototype plastic scintillating fibre microdosimeter with large similarities to the one intended to build in this work. The group built a detector system for beam monitoring, based on double cladding Kuraray SC-78 250 $\mu$m with a multilayer ribbon. The scintillating fibres were bonded with $TiO_2$ epoxy in a single layer and the overall thickness of the fibres plus the $TiO_2$ epoxy is approximately 1.2 mm. However, the authors claim that using two layer scintillating fibre stationed with epoxy would contribute almost 60% more to water

equivalent material than using the current system, based on multi-wire proportional counter beam monitor [40]. This increase on the water equivalent material is an unwanted effect, as it will increase the straggling and dispersion effects to the beam than what would be idealized. The system can be observed in figure 2.6.

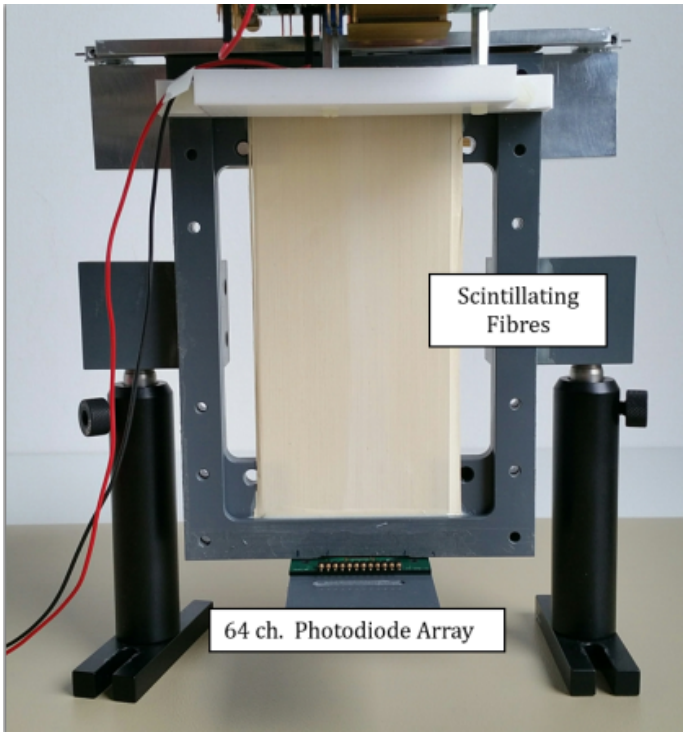


Figure 2.6: Detector system resulting from HIT research.The ribbons were 20 cm long and the width covered by the photosensor was 51.2 mm [41].

Scintillating Fibre–Optic Dosimeters (SFODs) present many advantages such as: measurement of the dose distribution with minimal perturbation, small sensitive volume, its robustness, that gas and high voltage are not required. The scintillation decay time is typically on the order of a few nanoseconds and the spatial granularity is proportional to the fibre's diameter, which can be as low as 0.25 mm for plastic fibres. The signal amplitude is proportional to the deposited energy in the fibre, though extensive research has shown this to be non-linear with increasing stopping power, dE/dx, for plastic scintillator [36, 40].

### 2.7.2 Tissue Equivalent Proportional Counter

The Tissue Equivalent Proportional Counter (TEPC) consists of a camera, generally a sphere or a cylinder, filled with a tissue equivalent gas [42] such as propane [43] or a mixture of methane, carbon dioxide and nitrogen [44], in which the variation of density is proportional to the energy radiation lost while traveling through the gas. The TEPC walls are made tissue equivalent to provide correct secondary particle spectra entering the gas.

For a tissue sphere of diameter $dt$, density $\rho_t$, and mass stopping power $(S/\rho)_t$ and a gas sphere with parameters $dg$, $\rho_g$, and $(S/\rho)_g$, the required condition of equivalent energy loss is:

$$\Delta E_t = (S/\rho)_t \rho_t dt = (S/\rho)_g \rho_g dg = \Delta E_g \tag{2.13}$$

where $\Delta E_t$ and $\Delta E_g$ are the mean energy losses from the charged particle in tissue and gas. The gas used must be also tissue equivalent. If the mass stopping powers are independent of density, then we have:

$$\rho_t dt = \rho_g dg \tag{2.14}$$

By adjusting the gas pressure and therefore the gas' density, it is possible to mimic the micron sized sensitive volume (SV) of tissue cell with a large gas volume [14].

Nevertheless, this type of detectors presents some disadvantages such as: having a large physical size and thus is only able to represent a unitary cell; it requires the supply of a gas, which can be expensive; requires a complicated correction process [45]. For instance, the wall effects which stem from the scattering of particles and production of secondary and tertiary particles lead to an increase in the energy imparted [37]. Finally they operate with high voltages, which can be dangerous [14].

In general, the proportional gas should not contain electronegative elements (i.e. oxygen) otherwise electrons heading towards the anode will combine with the gas [1, 44]. The gas in a proportional counter is usually a noble gas because it does not react chemically with the detector components. Of the noble gases, argon is the most widely used because of its low cost [44].

NASA developed a TEPC that is currently on-board the International Space Station (ISS) to characterize the radiation environment. This environment is characterized by mixed fields of high LET particles including protons and heavy ions. The purpose is to collect a record of the ISS environment to construct exposure history records for the crew. TEPC also provides near real-time measurements to ground personnel during radiation events as well as survey measurements in different parts of the ISS for shield verifications [43].

### 2.7.3 Si-based Microdosimeters

Si based microdosimeters rely on the use of a Metal Oxide Semiconductor Field Effect Transistor (MOSFET) which consists of three terminals: gate, source and drain. The source and drain terminals are made of a semiconductor, the gate terminal is made of metal and is detached from source and drain terminals using a metal oxide [46]. By applying a sufficiently high voltage to the gate, we are increasing the gap between the valence band and the Fermi level of the material, therefore current starts flowing, leading to the free movement of charges from the source to drain [36].

MOSFET based detectors measure the change in the threshold voltage necessary for current to flow between the source and drain. The threshold voltage changes as free electrons and holes are produced by ionizing radiation within the oxide layer. The change in threshold voltage is proportional to the absorbed dose [36].

Among the advantages of Si-based microdosimeters we highlight its small physical size (2-10 $\mu$m) and consequently its extremely high spatial resolution of up to 10 $\mu$m, which allows measurements near the Bragg peak and provides detailed assessment of dose mean lineal energy with depth, no gas-flow ensemble, operating at low voltages (10 V), high sensitivity [47] and the ability to replicate an array of cells [14]. Some of the disadvantages of this type of device are its temperature and dose rate dependencies, which require careful calibrations in order to produce accurate measurements. They are highly radio-sensitive therefore their ability to function as a detector deteriorates with accumulated dose, which requires the detectors to be periodically replaced. Finally, MOSFETs also exhibit angular dependency, which can lead to measurement errors in cases where the incident beam angle changes in relation to the detector [36].

The Centre for Medical Radiation Physics (CMRP) at the University of Wollongong, has been studying the implementation of a solid state microdosimeter on a single sensitive volume using a reverse biased p–n junction of the source diode in the n-type MOSFET. The group developed 5 generations of Si-based microdosimeters and found that there was a good agreement between the data obtained with Silicon on Insulator (SOI) microdosimeters and TEPC. SOI proved to be resistant even with high energy protons and ions [14]. In figure 2.7 we have an image of the median energy on each SV. It is possible to observe that most of the energy is deposited at the center.

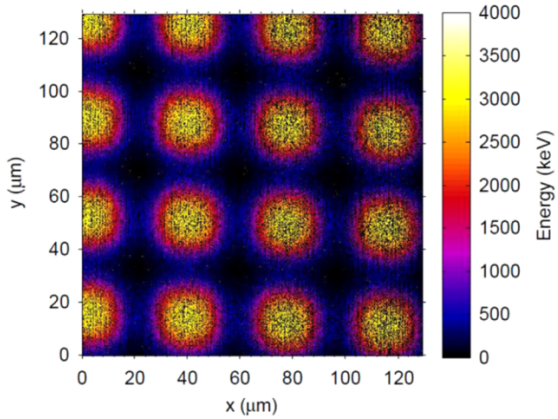


Figure 2.7: 2D map of the median energy of charge collection in a SOI [11]

Goméz *et al.* have also been involved in the development of silicon dosimeters and tested their efficiency by exposing it to an ion beam. The experimental results of lineal energy spectra were compared to those obtained through GEANT4 and FLUKA and the group found that there was excellent agreement between the experimental measurements and the simulations [11] as it is possible to see in figure 2.8.

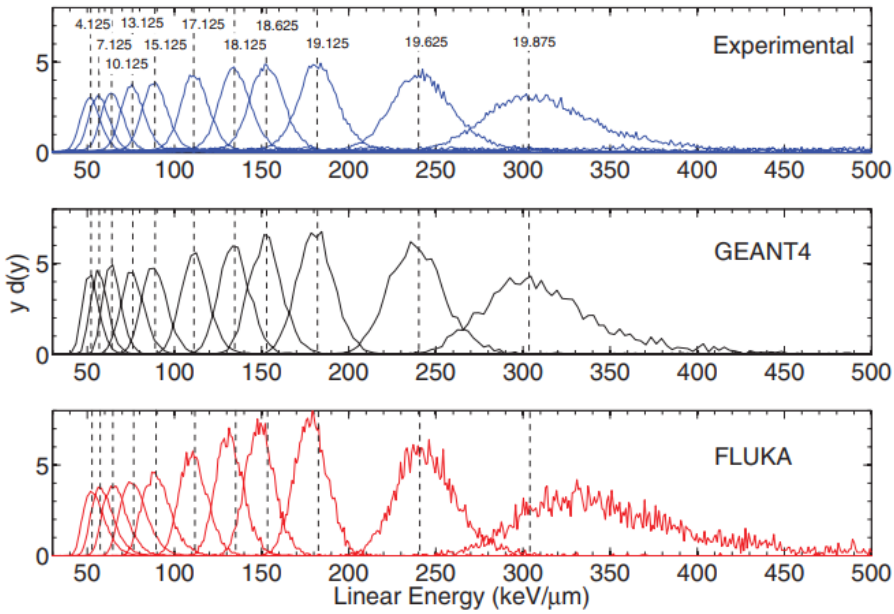


Figure 2.8: Microdosimetric distributions $yd(y)$ in silicon detectors from experimental data, FLUKA and GEANT4 at different depths in Lucite [11]

## 2.8 Silicon Photomultipliers

Silicon photomultipliers (SiPMs) are cell-structured, photo-sensitive semiconductors that have been replacing conventional photomultiplier in multiple areas such as high-energy, astroparticle physics [48] and have several applications for biomedical devices [49, 50].

SiPMs offer single-photon resolution allowing for a precise calibration of the incident light flux and have similar or higher photon detection efficiencies than conventional photomultiplier tubes (PMTs) [49]. In addition, they are tolerant against the exposure to bright light and offer a mechanically and optically robust design [48, 50]

## 2.9 Optical Fibres Overview

Over the last years, most of the research done with regards to optical fibre-based dosimetry concerns low dose applications. This research field is now quickly expanding to different applications such as those associated with high energy physics facilities [51], radiation test facilities, monitoring of nuclear power plants and even space missions [52].

Plastic fibres are comprised of a core and a cladding or multiple cladding. Multi cladding fibres have higher light yield than single cladding fibres because of its larger trapping efficiency [53]. Amongst other purposes, the cladding allows total internal reflection since the refractive index ($n_1$) of the core is larger than the index of the cladding ($n_2$) [36]. This process obeys to Snell's law.

$$\frac{n_1}{n_2} = \frac{sin\theta_2}{sin\theta_1} \tag{2.15}$$

This geometric property allows the imprisonment of light which can thus be transmitted over a substantial large distance. What's more, the cladding is useful to protect the core from abrasion or accumulation of foreign material [36]. Finally, using a multicladding layer over just one helps enhancing the efficiency of total reflection inside the optical fibre [54].

Using optical fibres as detectors has many advantages over other types of detectors such as high spatial resolution due to the small diameter of the optical fibre [40], the signal amplitude is proportional to the deposited energy, though it has been shown to be non-linear with increasing stopping power [36, 40]. Long-distant signal transmission and immunity to electromagnetic interference [45] (a characteristic especially useful in the medical environment) their robustness and flexibility.

## 2.10 Fluorescence Light Yield

When a scintillator is excited it emits light. This effect is called luminescence. There are several ways to excite a substance. For example, when it is excited with visible photons, it is called photoluminescence, whereas if it is excited by ionizing radiation, is called radioluminescence or scintillation [36].

The intensity of the signal $n(t)$ in photons as a function of time for plastic scintillators is expressed as:

$$n(t) = \frac{N}{\tau - \tau_R}[e^{\frac{-t}{\tau}} - e^{\frac{-t}{\tau_R}}] \tag{2.16}$$

Where $N$ are the photons that hit the scintillator, $\tau_R$ is the time necessary for the scintillator's response reach its peak, which is of the order of $10^{-9}$s, and $\tau$ represents the signal falloff, typically of the order of $10^{-8}$-$10^{-9}$ s [36].

Although most of the light reaching the light-measuring system is scintillating light, there is a portion of light which results from the stem effect within the optical fibre. The two main components causing the stem effect are fluorescence and Cerenkov radiation [36, 38]. While fluorescence is the property whereby a molecule or atom emits light with a higher wavelength than the one that caused the excitation [36, 55], Cerenkov radiation is produced when a charged particle's velocity exceeds the speed of light in a given medium [38]. Cerenkov radiation is generated at the core of the optical fibre, when the core has a refractive index greater than 1. Cerenkov is the main contributor to the stem effect in the fibre [36]. Since the plastic fibres are made of materials with low atomic number (Z), Cerenkov radiation is mainly produced by electrons through Compton interactions [36].

If irradiation conditions were always the same for every measurement, Cerenkov light would be a constant added to the output signal. Two different methods have been developed to filter Cerenkov induced noise. The first one relied on the use of two optical fibres. The first fibre would be of a scintillating material and second just a normal fibre.

By subtracting the signals, the Cerenkov would be successfully removed [36]. The second method depended on the use of filters. Since Cerenkov radiation is mostly emitted in the violet-blue region of the visible spectrum, several filter combinations were tested with a reduction of more than 50% of Cerenkov radiation [36].

From previous studies it is known that the signal produced from scintillation light rises linearly with both the radius and the length of the scintillator. However, increasing the size of a scintillator also increases the attenuation the light will undergo [38]. Therefore, there is always a trade-off between light production and attenuation.

### 2.10.1 Light Attenuation Coefficient

In a fibre-optic system there is a light attenuation factor which results in an optical power loss of the light that is propagated along the length of the fibre [36]. The attenuation coefficient of optical fibres has a logarithmic relationship with the power emitted, also known as Lambert-Beer law:

$$\frac{P_{out}}{P_{in}} = exp(-\alpha L) \tag{2.17}$$

The linear attenuation coefficient, $\alpha$, is influenced by a number of factors. As a main intrinsic factor we have Rayleigh scattering. Rayleigh scattering is caused by nonuniformities in the optical fibre and is the most common form of scattering [36]. Attenuation is also dependent on the core diameter of the fibre. It increases with the decrease of the core diameter, light rays strike more frequently on the interface between the core and the cladding, and this gives rise to higher attenuation. The attenuation coefficient also varies with the wavelength of the source and core material of the optical fibre [36].

It is possible to determine the attenuation coefficient experimentally. By plotting the signal detected at the readout system with the distance at which the optical fibre is illuminated from the readout setup and by doing an adequate fit to the curve, using equation 2.17 we can get $\alpha$.

## 2.11 Crosstalk

Crosstalk is the transference of radiation from one optical fibre to another adjacent fibre. This neighbouring fibre then absorbs or filters some of the transferred light. Consequently, there is a change in the absorption spectrum and cross contamination of the signal along the optical fibres [56].

In figure 2.9, curve (b) shows an enhancement of the shorter wavelength absorption. This is due to the coupling effect, which is wavelength dependent [56], and a consequent small shift of the absorption peak towards the short-wavelength end of the spectrum.

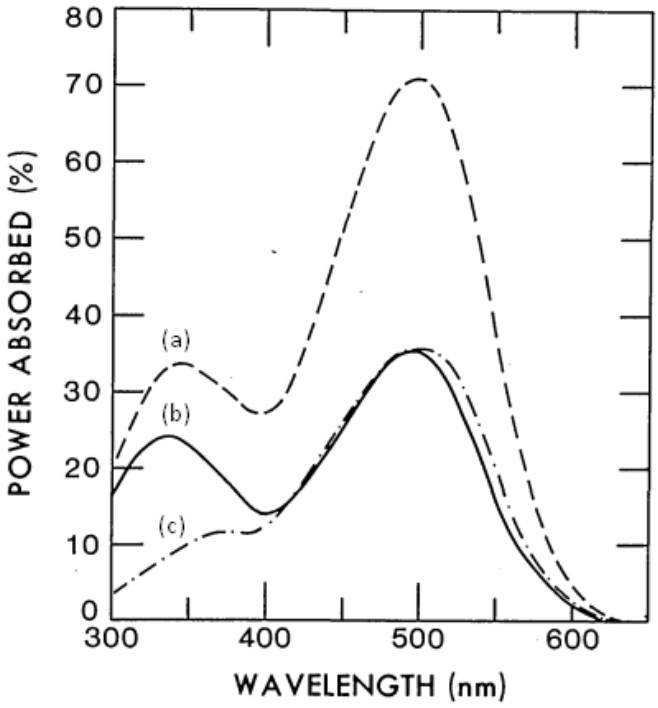


Figure 2.9: Percentage of the incident power absorbed (a) for an optical fibre in isolation (b) in the illuminated fibre, and (c) in the coupled fibre [56].

## 2.12 Quenching

Quenching is the variation of response of scintillators with the ionization density, which is the number of ions per unit of path length produced by a fast-charged particle along its track. This phenomenon is mostly due to the dissipation of energy by non-radiatively means and is associated with a reduction of the scintillation efficiency [36]. Many detectors suffer from LET-dependent quenching, such as silicon diodes [36].

Quenching is more significant when considering protons or heavy ions because the ionization density increases with depth [36]. As discussed in section 2.5, this kind of particles show an increase of energy deposition (Bragg's peak) at a certain depth. The increase in the energy deposition leads to a higher ionization density and therefore an increase in the quenching effect, causing a decrease on the signal intensity at the Bragg's peak [36, 39, 54] as it is represented in figure 2.10.

Quenching models are semiempirical because of the lack of comprehension of the physical process in scintillators; the most commonly used is Birk's model [36]. The light output yield per unit length, $\frac{dY}{dx}$, for a scintillator has been parameterized as a function of the stopping power as,

$$\frac{dY}{dx} = S\frac{\frac{dE}{dx}}{1 + kB\frac{dE}{dx}} \tag{2.18}$$

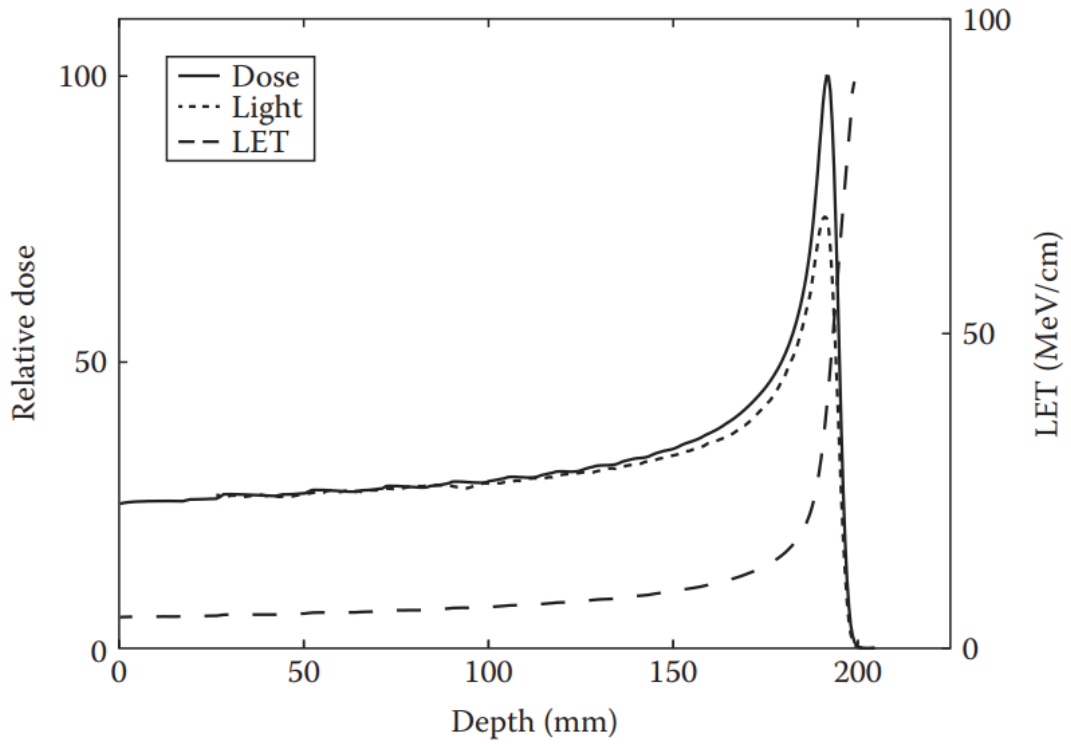


Figure 2.10: Light signal measured with an organic scintillator detector. The dose and LET were calculated using a Monte Carlo model [36].

where $S$ is the scintillation efficiency, which is defined as the fraction of energy absorbed by the scintillator by the total energy originally deposited, and $kB$ is the Birk's constant, characteristic of each material. Scintillation efficiency is strongly dependent on the particle type and energy, the response for electrons being higher than that for heavier particles such as proton and alpha particles for equivalent energies [57].

Outside the Bragg peak region, when $k_B \frac{dE}{dx} << 1$, the light yield is proportional to the stopping power (or LET),

$$\frac{dY}{dx} = S\frac{dE}{dx} \tag{2.19}$$

Since the stopping power, $\frac{dE}{dx}$, in the Bragg peak is very high, the saturation occurs along the particle's track [36]. In that regime, the Birk's formula can be written as:

$$\frac{dY}{dx} = \frac{S}{k_B}. \tag{2.20}$$

Chapter 3

# Methods & Materials

In this chapter the methodology and tools used to study the optical properties of scintillating optical fibres are presented.

## 3.1 Scintillating Fibres

The optical fibres used were manufactured by Kuraray, Japan. These were plastic scintillating (SCSF-78), multi cladding fibres. The diameters of the fibres used in this work were 1 mm, 500 $\mu$m and 250 $\mu$m. The total thickness of the claddings could vary between 4% up to 6% of the total diameter of the fibre [53]. In figure 3.1 it is possible to find a schematic representation of the optical fibres.

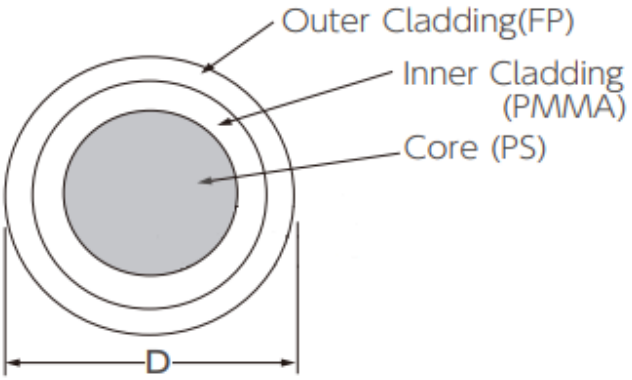


Figure 3.1: Representation of the cross section of the scintillating optical fibres used [53].

In table 3.1 it is possible to consult the list of materials the optical fibre is made of, their density, refraction index and atomic density.

Table 3.1: Physical properties of the different constituents of the optical fibre [53].

| | | Materials | Refracting Index | Density (g/cm$^3$) | No. of Atoms per cm$^3$ |
|---|---|---|---|---|---|
| Core | | Polystyrene (PS) | 1.59 | 1.05 | C: 4.9x10$^2$2 H: 4.9x10$^2$2 |
| Cladding | for single cladding inner for multi-cladding | Polymethylmethacrylate (PMMA) | 1.49 | 1.19 | C: 3.6x10$^2$2 H: 5.7x10$^2$2 O: 1.4x10$^2$2 |
| | outer for multi-cladding | Fluorinated polymer (FP) | 1.42 | 1.43 | |

## 3.2 Optical Fibres Support System for Output Readout

At LIP's laboratory, LOMAC (Laboratório de Óptica de Materiais Cintilantes), there is an equiment named "fibrometer" built to measure the fibres' light output yield. With this equipment it is possible to estimate, for instance, the attenuation coefficient. This machine has been previously used to measure the yield output of the optical fibres used at the TileCal detector ATLAS [58], one of the four detectors of the LHC experiment in Switzerland.

The fibrometer's general setup consists of a source of light at one end and a photomultiplier (PMT) at the other (see Fig. 3.2). In between, one can place the fibres to be analysed in single fibre grooves. The fibrometer has a XY table that allows for the automatization of the signal-reading process [58]. While the X motor moves the LED through the length of the optical fibres, the Y motor moves the table that contains the tray with the fibres.

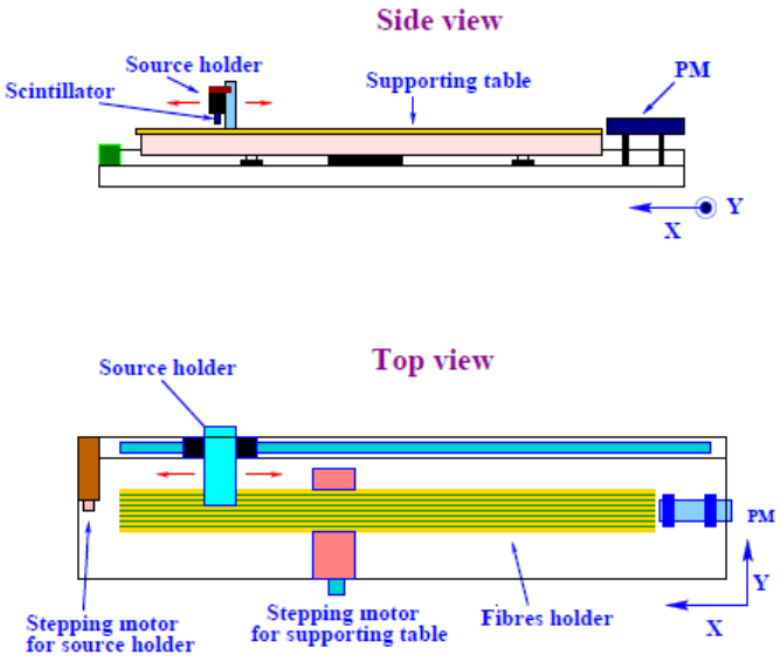


Figure 3.2: Schematic representation of the transverse and longitudinal view of the fibrometer [58].

The light readout system of the fibrometer consists of a blue sensitive EMI 9813KB PMT air coupled to a light mixer. The signal from the PMT is read by a KEITHLEY 485 auto-ranging picoammeter, equipped with a KEITHLEY 4853 IEEE488 interface [58]. The

PMT and light mixer are enclosed in a cylindrical metallic case with a 300 $\mu$m slit in the center. These slits work as a filter for unwanted radiation and its width can be adjusted.

Since we wanted to quantify crosstalk effect in adjacent optical fibres, it was necessary to adapt the setup to our problem. Therefore, a new tray was designed with specific characteristics that would meet our needs. These were:

- Multi-fibre grooves - New grooves were designed to accommodate several juxtapose fibres as well as singe fibre grooves.
- Isolation - One of the main motivations to create this new support was to isolate the array of fibres from any other light source, especially from neighbouring LEDs.
- Materials - Given that one of the purposes of this support was to study the crosstalk effect between the optical fibres, the material of the support had to be non-reflecting (opaque), therefore POM (Polyoxymethylene) was the material chosen.
- Dimensions - The tray could not exceed the fitting dimensions of the platform that would fix the tray to the fibrometer.
- Versatility - The support was designed so that it could accommodate a variable number of optical fibres with different diameters. This was accomplished by cutting grooves with different depths (1 mm, 500 $\mu$m and 250 $\mu$m).
- Baseline - To control the lighting conditions of the system, an extra groove was added for each fibre diameter. This acted as a measurement of the baseline and as a control factor.

The first drafts of the tray were designed using Fusion 360 and were later sent to a workshop in LIP Coimbra to be further discussed and validated.

## 3.3 Characterization Techniques

### 3.3.1 Raman Spectroscopy

One of the tasks of this work was to identify which polymers are present in the scintillating fibres. This was done by acquiring the Raman spectrum of a fibre and then identifying the different compounds by comparison with references.

Raman spectroscopy is a technique based on inelastic scattering of monochromatic radiation [59], usually a laser [59, 60]. When photons interact with a sample, they are scattered and remitted with a different frequency. This shift in the frequency of the photons is called the Raman effect and it provides information about vibrational, rotational and other low frequency transitions in molecules.

When photons hit the sample, their electric field and the electrons of the molecules of the sample interact, producing a magnetic dipole and consequently the molecules start

to oscillate. When this oscillation causes a variation in the polarizability of the molecules Raman active vibrational (or rotational) modes are induced [60]. The bands observed in a Raman spectrum are the vibrational modes of the molecule for which the condition mentioned previously is verified. Each vibrational state has a corresponding wave number ($cm^{-1}$) associated, making it possible to identify bonds and therefore compounds.

In order to obtain a signal as intense as possible, various factors are important: the intensity of the laser beam, the number of molecules that are irradiated and the collection of the Raman diffused light which should be as efficient as possible [61]. When performing micro-Raman spectrometry, the radiation collection efficiency is greatly influenced by the lens, which should have a transmission coefficient as high as possible [61]. An important parameter of the lens is the Numerical Aperture (N.A.), which describes the size of a conical beam of light that can pass through a lens. This quantity can be calculated as:

$$\text{N.A.} = n \times sin(u) \tag{3.1}$$

with $n$ the refractive index of the medium and $u$ the half top angle of the light cone. In figure 3.3 we can find a schematic representation of this relationship.

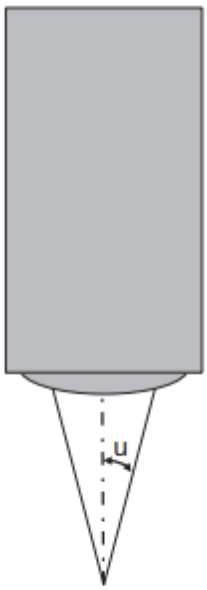


Figure 3.3: Schematic drawing of the aperture cone of an objective lens [61].

An important practical aspect of the Raman technique in this work has to do with the photon capture. In a micro-Raman system there is always a slit entrance into the spectrometer, which can be adjusted in terms of its diameter, and a microscope with various lenses that differ on their N.A. In between the microscope and the slit, it's possible to install a confocal pinhole, to further reduce the probed volume, which is what we have in our Raman spectrometer. Figure 3.4 is a schematic of the two setups described.

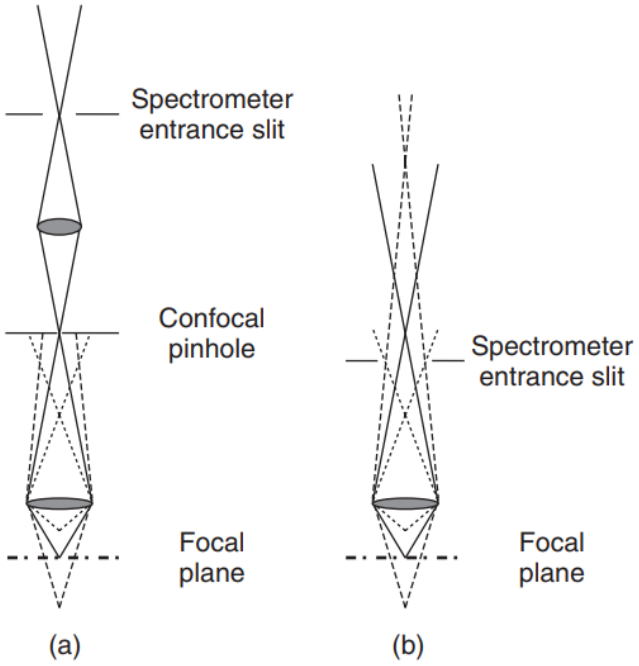


Figure 3.4: Scheme of a confocal (a) and a conventional (b) microscope, coupled to a spectrometer [61].

In the simplest setup, when there is only the slit without the confocal pinhole, the laser beam is led into the microscope unit, whereby the microscope objective is used as focusing lens. The same lens is used to collect and send the diffused light to the spectrometer [61]. A big disadvantage in this setup is that the signal (peak) to noise is not optimal in most cases as there is a significant amount of photons being captured from other planes.

In the setup with the confocal hole, the assembly isolates the light from a specific plane in the sample which coincides with the illuminated part, and eliminates the radiation efficiently coming from other planes which are out of focus. With this setup it is possible to avoid the Raman signal and the fluorescence contribution of areas which are not in focus [61].

The lateral resolution $\delta_p$ of a Raman spectrometer is given by:

$$\delta_p = 1.22 \times \frac{\lambda}{\text{N.A.}} \tag{3.2}$$

with $\lambda$ being the laser wavelength and N.A. the numerical aperture of the lens. This limit value, however, is not reached in practice [61]. Besides the lateral resolution, the depth resolution also plays an important role. An approximate formula for the depth resolution is given by:

$$\delta_z \geq \left| \frac{4.4n\lambda}{2\pi(\text{N.A.})^2} \right| \tag{3.3}$$

The spectrometer used in this work was a confocal micron-Raman from XploRA (Horiba/jobin-Yvon Xplora, France) coupled with an Olympus microscope with three different resolutions: 10x, 50x, 100x. The source of light was a laser with an approximate wavelength of 785 nm [60].

### 3.3.2 Spectrophotometry

Spectrophotometry is a method to measure how much light is absorbed by a substance for different wavelengths. The basic principle is that each compound absorbs or transmits light over a certain range of wavelength [57]. This measurements are in percentage relatively to the sample without any films.

Transmittance is the fraction of light that passes through the sample. This can be calculated using the equation:

$$\text{Transmittance } (T) = \frac{I_t}{I_0} \tag{3.4}$$

Where $I_t$ is the light intensity after the beam of light passes through the sample and $I_0$ is the light intensity before the beam of light passes through the sample. Transmittance is related to absorption by the expression:

$$\text{Absorbance } (A) = -\log_{10}(T) = -\log_{10}\left(\frac{I_t}{I_0}\right) \tag{3.5}$$

## 3.4 Film Deposits

During this work it was also studied the possibility of applying an extra film to reduce crosstalk effect between optical fibres. Ideally this coating should be transparent to light and help increase the light capturing effect. With the current setup it was possible to use two different deposition techniques, which will be explained briefly in the following sections.

### 3.4.1 Magnetron Sputtering

Sputtering is a process whereby atoms or molecules of a material are ejected from a target by bombardment of high-energy particles [62]. To bombard the target, an electrical discharge is applied to a gas. This discharge, created by low pressures ($10^{-1}$ to $10^{-3}$ mbar) and high voltage, ionizes the gas, forming accelerated positive ions (plasma) [63, 64]. These ions hit the target as they are accelerated by the electrodes and material is ejected

from the target [62]. This discharge also depends on the gas ejected in the chamber. Generally, a noble gas is used so that only the material of the target is deposited onto the substract, although other gases can be used, such as oxygen, to form oxides.

Sputter coating is a vacuum process, as low pressures are required to maintain high ion energies and to prevent too many atom-gas collisions after ejection from the target. There are several physical quantities that influence the quality of the film such as the pressure of the chamber, the tension applied between the electrodes, the distance between the electrodes,the gas used to create the plasma, the current and the power.

The breakdown voltage for which there is a gas discharge is a function of the product of the pressure and gap length between electrodes. This empirical law is called Paschen's Law, named after the scientist that first observed this relationship. Hence, the minimum voltage required to ignite the discharge of a gas sample of pressure $p$ over a distance $d$ is as:

$$V_B = \frac{Bpd}{\ln(Apd) - \ln\left(\ln\left(1 + \frac{1}{\gamma_e}\right)\right)} \tag{3.6}$$

Where $\gamma_e$ is the secondary-electron-emission coefficient and $A$ is saturation ionization in the gas, $B$ is a constant related with the excitation and ionization energies [65].

In our setup there was a magnet behind the target. The magnetic field generated helped maximize the number of electron-ion collisions in the gas, increasing the number of collisions electrons-gas molecules and therefore increasing the overall bombardment of the target. This magnetic field also helps reduce the bombardment of the substract by the electrons by confining the plasma and therefore reducing the voltage applied as well as the working pressure [64].

### 3.4.2 Thermal Evaporation

The system mentioned previously also accommodates another different kind of deposition process - Thermal evaporation. In this technique, which is a direct application of Joule effect, the material that is to be deposited evaporates and once it finds a surface it condensates, forming a thin film [66].

Firstly the deposition material is placed in the coils of a tungsten compact resistance. Before initializing the deposition process, the chamber is sealed and the pressure is dropped until values of high vacuum ($10^{-5}$ to $10^{-6}$ mbar) to clear the chamber of residual particles, allowing the film to be purest possible [66]. After the chamber's pressure has dropped to an optimal working value, the source for current supply is turned on and high currents heat up the resistance to the point it gets incandescent. At this point the deposition material should start fusing and evaporate isotropically. Once the process is over, the chamber is slowly depressurized until the atmospheric pressure so that the films cool down slowly until the temperature of the room.

This technique has some limitation such as controlling the thickness of the deposited film as well as having some contamination from the resistance [66], but it is also possible to identify some advantages namely this process being simpler, quicker and being overall cheaper when compared with magnetron sputtering.

## 3.5 Simulations

The Monte Carlo simulations were done using FLUKA, a tool developed by CERN (Conseil Européen pour la Recherche Nucléaire) which can simulate with high accuracy several types of particles with energies that range from 1 keV to thousands of TeV [67]. Flair is an advanced user friendly interface for FLUKA which facilitates the editing of FLUKA input files, execution of the code and visualization of the output files. It is based entirely on python and Tkinter [67].

FLUKA reads an .inp which has all the system described by means of cards. You can define your beam, the geometry, correction factors, specific physics libraries as well as choosing the number of particles that are tracked and how the data is stored. Data storage is defined by the card USRBIN. For this work we used USRBIN by cartesian coordinates and by Region. In cartesian coordinates it is necessary to define the limits for each coordinate and then to pick the number of bins. When you define the USRBIN by Region you look at the geometries objects.

For the simulations the range considered for charged particles, the protons, was continuous slowing down approximation range (CSDA). This approximation considers a continuous loss of energy equal to the energy lost over a unit of length, LET, being that this does not account for fluctuations in energy losses mostly because of how LET is defined as it was explained in section 2.1.2.

# Chapter 4

# Results & Discussion

## 4.1 Fibres' Composition

As it was previously mentioned in section 3.3.1, a Raman spectrometer was used to identify the compounds of the fibres. We started by acquiring the spectrum of samples that had a similar composition of the materials that constitute the fibres. These were polystyrene and PMMA (two slabs), which can be observed in figure 4.1a and figure 4.1b respectively.

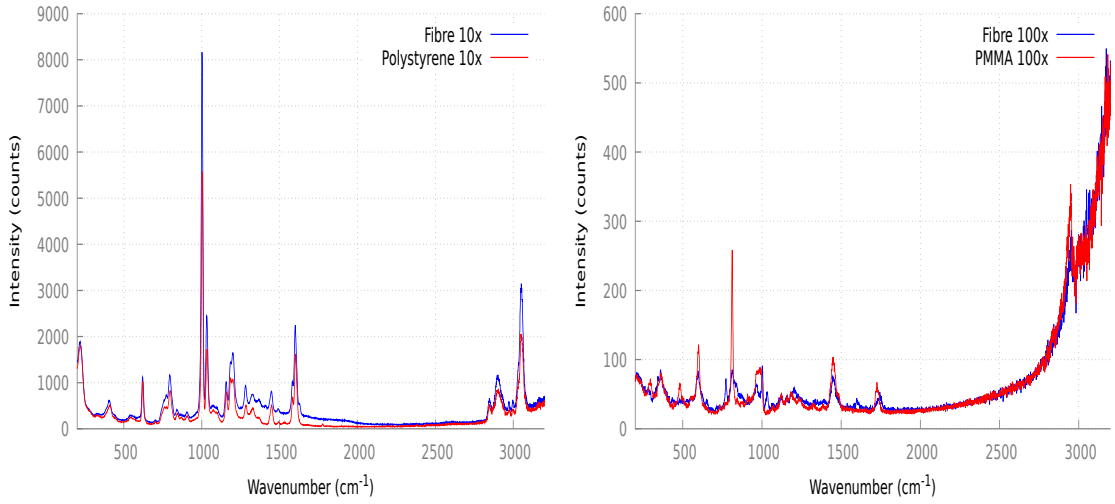


(a) Overlap of the Raman spectrum of a fibre with a 10x magnification with PS with a 10x magnification.

(b) Overlap of the Raman spectrum of a fibre with a 100x magnification with PMMA with a 100x magnification.

Figure 4.1: Raman spectra obtained for the optical fibre and the slabs.

We found that using different ampliations when acquiring the Raman spectrum of

the scintillating fibres, we would get different spectra. This was related with the focal plane and the probed volume observed and that ultimately had to do with the lens being used. With a resolution of 10x we are observing a large volume of molecules, and since the cladding only makes up about 4% of the total diameter of the optical fibre [53], the claddings' signal is less intense when compared with the PS core. As for the resolution of 100x, the spectrum obtained is different. It seems to be a mix of two different compounds: PMMA and the fluorinated polymer, which are the materials that constitute the claddings. Considering what was said previously, the rationale is the same. In this case we are observing a smaller volume and it is easier to have the focal plane on the cladding, thus obtaining a signal focused on the claddings.

Table 4.1: Raman spectroscopy peaks in $cm^{-1}$ for the scintillating fibre with an ampliation of 10x and for a slab of polystyrene and the Raman bands according to the literature for PS [68].

| Fibre 10x | Polystyrene | Literature | Bond |
|---|---|---|---|
| 219 | 219 | | |
| 411 | 406 | | |
| 620 | 621 | | |
| 794 | 797 | 800 | C——C |
| 1001 | 1004 | 1000 | C——H |
| 1038 | 1036 | | |
| 1154 | 1156 | | |
| 1199 | 1185 | | |
| 1282 | 1282 | | |
| 1448 | 1449 | | |
| 1579 | 1582 | | |
| 1601 | 1602 | 1600 | C═C |
| 2845 | 2847 | | |
| 2902 | 2905 | 2900 | C——H (aliphatic carbon) |
| 3050 | 3052 | 3050 | C——H (ring) |

By overlapping the spectrum obtained for the optical fibre with a lens 10x and the slab of PS it is possible to observe a near identical match in the spectra. From table 4.1 it is clear that the material observed for this Raman acquisition is polystyrene since there is little deviation in the wavenumber.

Table 4.2: Raman spectroscopy peaks in $cm^{-1}$ for the fibre with an ampliation of 100x, for a slab of PMMA with both ampliations of 10x and 100x and Raman bands according to the literature for polyvinylidene fluoride [68, 69].

| Fibre 100x | PMMA 100x | PMMA 10x | Literature PMMA | Bond PMMA |
|---|---|---|---|---|
| | 294 | 296 | | |
| 340 | | | | |
| 360 | 364 | 362 | | |
| | 483 | 482 | | |
| | | 556 | 562 | C——O |
| 597 | 599 | 601 | 597 | C——O |
| 655 | | | | |
| | 733 | 736 | | |
| 772 | | 770 | 770 | C——$H_3$ |
| 810 | 814 | 813 | | |
| | | 913 | | |
| | | 966 | | |
| 1002 | 994 | 987 | 998 | O═C═O |
| 1034 | | | | |
| | 1121; 1158; | 1124; 1156 | 1100 -1160 | Band Pattern |
| 1201 | | | 1190-1210 | |
| | 1235 | 1239 | 1231 | C——O |
| | | | 1050-1300 | |
| | 1325 | 1322 | | |
| 1446 | 1384; 1451; 1482 | 1389; 1450; 1482 | 1350-1500 | Methylene |
| 1741 | 1724 | 1726 | 1730 | C═O |
| 2953 | 2949 | 2836; 2874; 2948; 3002 | 2800-3100 | C——H |

The spectrum obtained for the scintillating fibre with a lens 100x and the slab of PMMA are a close match. Although there are multiple matches with PMMA, in the literature of flourinated PMMA, it says that the C═O stretching vibration, which in PMMA lies at about 1730 $cm^{-1}$, is raised to higher frequencies in the flourinated PMMA due to the presence of fluorine atoms in the molecule [70], which is coherent with our results. In another article characterising fluorinated polymers we found other bonds which are a match with our spectrum such as that for 648 $cm^{-1}$ corresponding to CCF+CC [69].

Considering that these optical fibres had a double cladding, we believe there is a middle coating of PMMA and an outer layer of flourinated PMMA, although more testing

would be necessary, especially to evaluate the infra-red spectrum of each material, as it would give extra information about the chemical bonds.

## 4.2 Light Yield

In order to measure the light yield the previous setup for fibrometer was used. However, it was still necessary to choose a LED that emitted light in the wavelength at which the scintillating fibres had its emission peak, which is 450 nm [53]. Thus, several UV LEDs were tested with the optical fibre to see whether the fibre emitted on the mentioned emission peak, as well as seeing the operating conditions (voltage and current) of the LED. The results can be found in table 4.3.

Table 4.3: Measured intensity and wavelength using a spectrometer values for different LEDs illuminating the fibre perpendicularly in optimal current and voltage parameters at approximately 12.5 cm from the light guide.

| | Current (mA) | Voltage (V) | Intensity | Emission Peak (nm) |
|---|---|---|---|---|
| RLS-UV385 | 9 | 3.095 | 4737 | 450 |
| RLS-UV370E | 15 | 3.424 | 2320 | 450 |
| RLS-UV380 | 11 | 3.384 | 4353 | 450 |
| NS 375 | 13 | 3.484 | 4001 | 450 |
| NS 360 | 15 | 3.489 | 2622 | 450 |
| RLT 360 | 14 | 3.828 | 2500 | 452 |
| RLT 365-525 | 12 | 3.858 | 2278 | 455 |

The set of LEDs chosen were the RLS-UV385 since these LEDs produced a higher intensity of signal in the scintillating fibre for lower current and voltage parameters, and the peak corresponded to the fibres wavelength emission peak [40].

To analyse the light yield of the fibres 8 scintillating fibres were individually studied. During the scans, there was a fibre that works as our baseline to evaluate the system's stability which we will call fixed fibre. The fibres were in the following arrangement from left to right: one fix fibre, 4 scintillating fibres of 1 mm, 2 scintillating fibres of 500 $\mu$m, 2 scintillating fibres of 250 $\mu$m and lastly a Wavelength Shifter (WLS) fibre. They all were one meter long, except for the fix fibre and the WLS fibre, which were two meters.

Two different set of measurements were made: one transversely to the tray, for the different fibres' diameters, and a longitudinal, along the fibres' length. In figure 4.2 we can find the results for the transverse scan. These results are coherent with what was said in section 2.10 that scintillation light rises with the radius of the optical fibre.

As for the longitudinal scan the results can be found in figure 4.3. In here, there are three sets of data and their respective fit with matching colour.

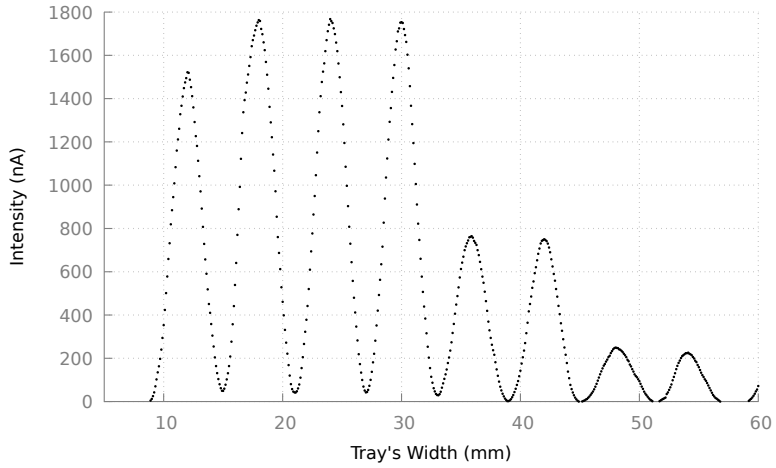


Figure 4.2: Plot of the signal intensity versus the Y position relative to the fibres' tray.

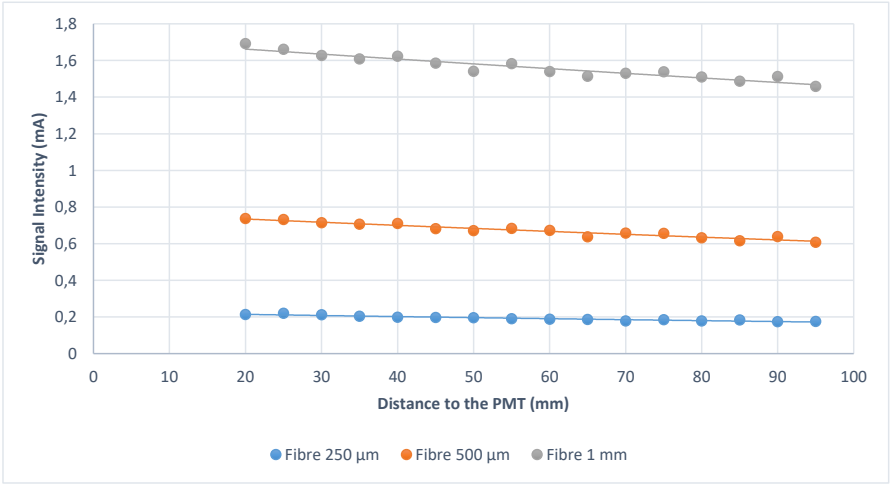


Figure 4.3: Signal intensity versus the fibres' length.

### 4.2.1 Linear Attenuation Coefficient

As explained in section 2.10.1, it is possible to obtain the linear attenuation coefficient by doing an exponential fit to the intensity of light according to the length of the scintillating fibre. The expressions obtained with the experimental measurements and their respective $R^2$ and Mean Squared Error (MSE) are presented in table 4.4.

Table 4.4: Results obtained from the exponential fit applied to each scintillating fibre, their $R^2$ and attenuation coefficient with a RLS-UV385 LED with applied tension of 2.77 V.

| **Fibre** | **Fit** | **$R^2$** | **Attenuation Coefficient ($cm^{-1}$)** | MSE |
|---|---|---|---|---|
| 1 mm | $1,718e^{-0,0017x}$ | 0,903 | $(1.7 \pm 0.2)\times10^{-3}$ | 0,0004 |
| 500 $\mu$m | $0,771e^{-0,0024x}$ | 0,925 | $(2.4 \pm 0.2)\times10^{-3}$ | 0,011 |
| 250 $\mu$m | $0,227e^{-0,0029x}$ | 0,921 | $(2.9 \pm 0.2)\times10^{-3}$ | 0,0068 |

We knew that light responses versus the fibre's length is well modelled by an exponential fit, as mentioned in section 2.10.1. From our results we observe that the attenuation coefficient increases with decreasing core diameter. The results are also in line with the theory in regards to attenuation's relationship with the diameter of the core.

R-squared is a statistical measure of how close the data are to the fitted regression line. For our data, the R-squared value was always above 90% indicating that the fits were adequate to our data. MSE was calculated and what we verified was that the fit for fibres of 1 mm had the worse $R^2$ but lowest MSE, whereas 500 $\mu$m had the best $R^2$ and worse MSE. This means that the fit for fibres of 1 mm is slightly worse than the other fits, but the variation between the measurement and the fit are less deviated. The least square method was used to compute the error of the coefficient values. From previous studies [58] the error of this measurements was about 4% so there was an overall increase of the error, probably due to the system losing its stability over time.

## 4.3 Crosstalk

### 4.3.1 Optical Fibres' Tray

As mentioned previously, a tray was especially designed to quantify the crosstalk effect between adjacent optical fibres. Several sketch iterations were made to optimize the signal readout from the optical fibres. It is possible to find the final sketches in annex I.

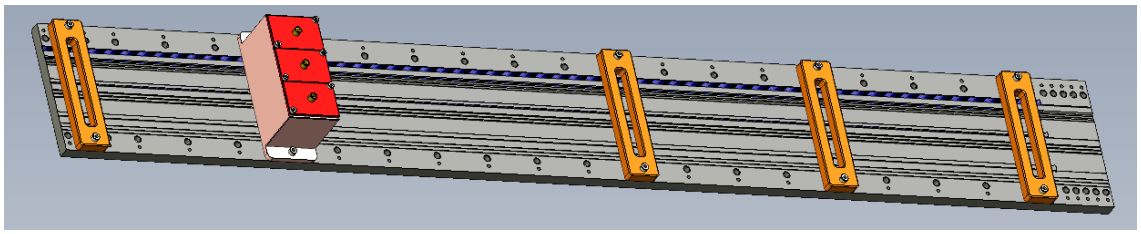

Figure 4.4: Render of the tray with the support pieces.

In figure 4.4, we can find the rendered final version of the tray. The tray is 1050 cm long, 130 wide and has a height of 10 cm. The tray accommodates all three different fibre diameters, 1 mm, 500 $\mu$m and 250 $\mu$m simultaneously. Each groove has a width of 5 mm, and next to it there are 3 separate grooves with fibre-specific diameter that work as a baseline for the measurements. This is possible to observe in more detail in figure 4.6. In this figure there is also another important feature of this tray. There is the possibility to have an optical fibre being illuminated without having any neighbouring optical fibres, and once the light reaches the point where there are multiple fibres, to see how much light is transmitted from the core to the adjacent fibres.

One thing to be considered was the possible overlap of signal coming out from the edge of optical fibres in adjacent grooves. To avoid that, the minimal distance at which the groves had to be from one another was calculated. We know that the exit angle for

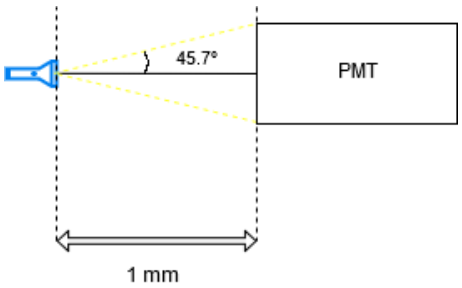


Figure 4.5: Schematic representation of the N.A. and its possible influence in the crosstalk effect.

light coming out of the optical fibre is 45.7° [53], and that the distance from the fibre to the PMT is roughly 1 mm, using the mathematical expression that describes the tangent, we get that the opposite edge should be wider than 1,024 mm. Because this is only half of the aperture, it is necessary to multiply this value by 2, giving 2,049 mm. This value is the minimum value necessary between different groups of fibres so that there is no interference in the signal that we wish to read. Check figure 4.5 to get a better understanding of what was just explained

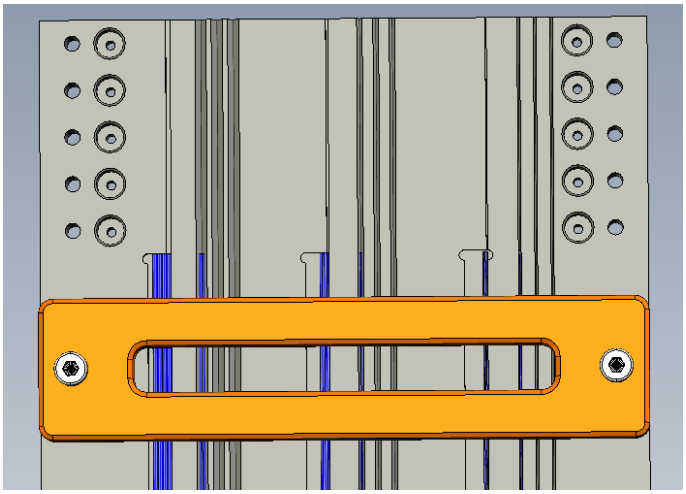

Figure 4.6: Zoomed in view of the tray.

The orange pieces placed in the tray work as fasteners to keep the optical fibres tight and also to exert some compression, as the fibres might be slightly bended by the way they are packed to be shipped. Figure 4.4 also shows a red box that accommodates the LED supports with associated electronic circuit and it is possible to insert 3 modules of LED supports, making a total of 6 LED capacity. In the tray there are two kinds of holes, one for the orange fasteners and for the LED support box (the outer most), and another which its sole purpose is to guarantee maximum light isolation by having an extra precision fitting for the LED support box.

Finally, in figure 4.7 we can analyse the LED support in more detail. This module was

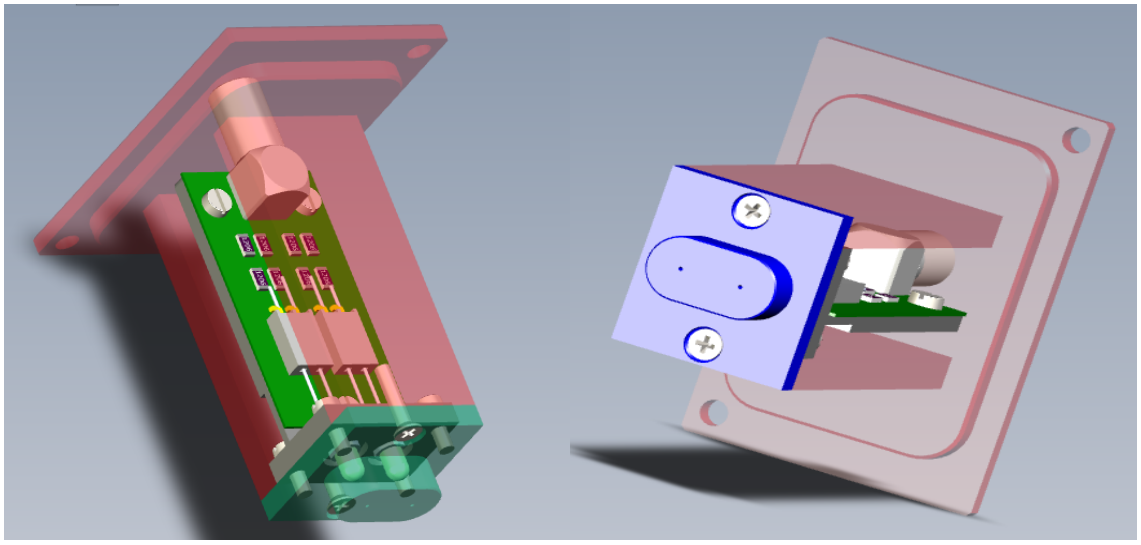

(a) Front/side view of the LED support. (b) Bottom/side view of the LED support.

Figure 4.7: Set of figures of the LED support. This support fits into the red box from figure 4.4.

projected so that it would be possible to easily access the circuit and substitute any electronic component if necessary. Each of these modules contains a small board connected to a power supply by a connector. In figure 4.7a the blue piece that contains the LEDs is made so that each LEDs light does not interfere with one another. There are pinholes of varying sizes (size of the fibre's diameter) all the way down to guide the light and reach the optical fibre.

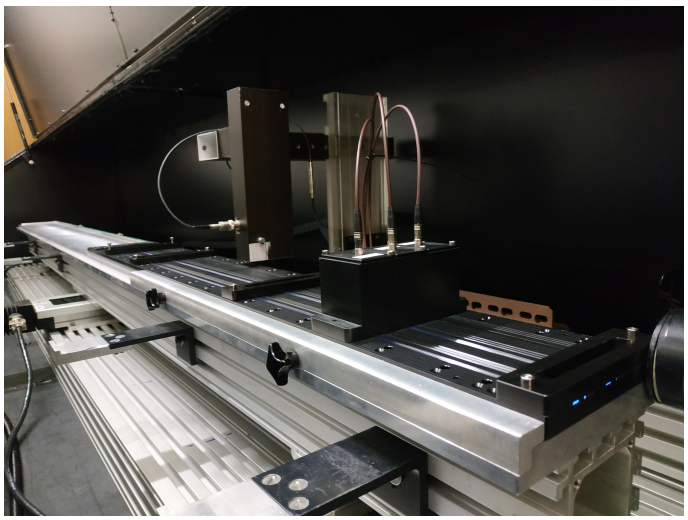

Figure 4.8: Photograph of the experimental setup for the crosstalk measurements.

### 4.3.2 Measurements

In the first steps of the determination of the crosstalk effect it was mandatory to create a experimental protocol in order to maintain as much as possible the initial conditions for every measurement.

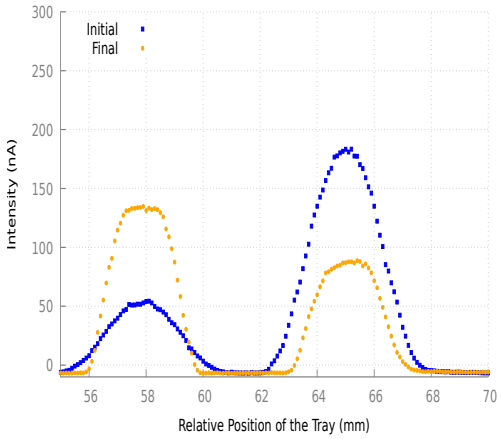


a Transverse light yield in LED swap setup.

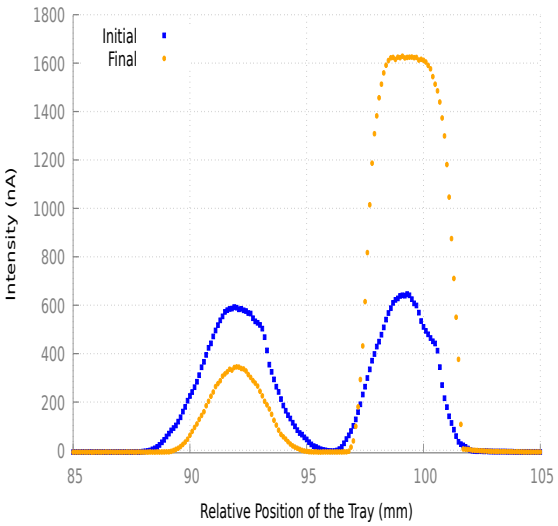


b Transverse light yield in LED swap setup.

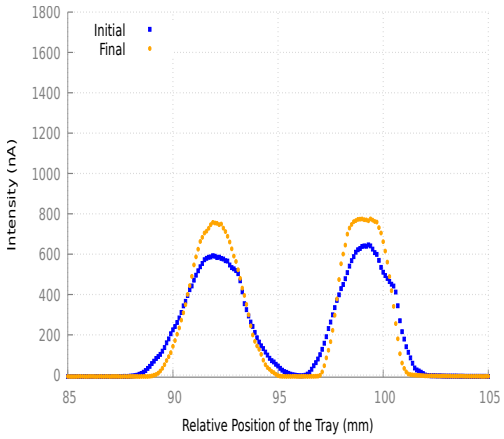


c Transverse light yield in PMT-tray positioning adjustment setup.

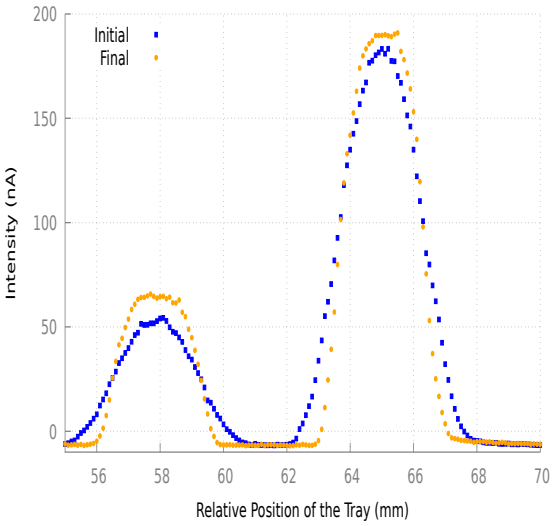


d Transverse light yield PMT-tray positioning adjustment setup.

Figure 4.9: Light output for each measurement. On the right: 1 fibre of 500 $\mu$m, between 56 and 60 cm and between 62 to 68 cm we have the signal for 10 fibres. Left: scintillating fibres of 1 mm, between 90 and 95 and between 97 to 103 cm we have the signal for 5 fibres.

We formulated tests to understand the degree of reproducibility of the results. The first one was the swap the LEDs of the module, by rotating the module 180 degrees. The results can be found in figure 4.9a and 4.9b. We can see the clear effect of almost 3

orders of magnitude LED swapping has on the output yield of the 500 $\mu$m fibres. Even though the LEDs came from the same batch, it is possible that they slightly differ from one another. This difference in signal might also have to do with the embedded circuit created for the modules, which might have some connectivity problems. However, if we look at results in figure 4.9b, initially, we had the same signal intensity for the grouped and isolated scintillating fibre and when we swapped the LEDs we started observing the same effect as we have in 1 mm fibres. In fact, in the next measurement we decided to swap the LEDs again and this pattern remained.

When we approximated the tray to the PMT, for almost 1 mm, we obtained the results in figure 4.9d and 4.9c. There is a slight increase in the overall light yield, and the shape of the peak narrowed, although the maximum became more of a plateau.

## 4.4 Film Deposits

For several years now, LIP has been involved in the aluminization of plastic optical fibres, and it is of general consensus that aluminium does not adhere well to polymers. Nevertheless, aluminium is a good final coating material because of its mirror-like reflectivity which diminishes the effect of crosstalk and increases the gain of the signal.

In order to address the adherence issue, two intermediate coatings were tested. These would act as a glue agent between the aluminium and the optical fibre. The intermediate deposits were ZnO and $TiO_2$.

### 4.4.1 Magnetron Sputtering

For this process it was established that the PMMA and PS slabs were put side by side, underneath the cathode, although the PS slab was the most centred with the cathode. Before any deposition, the slabs were carefully cleaned with Isopropyl alcohol and ultrapure water. The ultrapure water with a resistivity of 18 M$\Omega$ cm was supplied by a Millipore system (Milli-Q, Millipore GmbH).

$TiO_2$, ZnO and Al films were deposited at room temperature onto gold interdigitated by DC (voltage source, Huttinger PFG 10000) magnetron sputtering in a custom-made system. A titanium, zinc and alumininium discs (Goodfellow, 99.99% purity) with 64.5 mm of diameter and 4 mm of thickness each were used as sputtering targets. A turbomolecular pump (Pfeiffer TMH 1001) was used to achieve a base pressure of $10^{-4}$-$10^{-5}$ Pa [66]. Before the sputter-deposition step of the films, a movable shutter was interposed between the target and the substrates. The target was pre-sputtered in Ar atmosphere for 2 minutes to clean the target surface. The target-to-substrate distance was kept constant at 100 mm. Gases in the system were pure Ar and $O_2$ and their partial pressures were separately controlled by needle valves. Table 4.5 summarizes the sputtering conditions.

For ZnO several conditions were tested since it was not known what the optimal parameters were to get a quality film. It was observed that for deposition conditions

Table 4.5: Parameters during sputtering deposition.

| | Power (W) | Current (A) | Tension (V) | Pressure (mbar) | $\%O_2$ | %Ar | Deposition Time (min.) |
|---|---|---|---|---|---|---|---|
| ZnO_1 | 520 | 1.14 | 458 | $2.0 \times 10^{-2}$ | 100 | - | 20 |
| ZnO_2 | 130 | 0.36 | 369 | $5.0 \times 10^{-2}$ | 100 | - | 10 |
| ZnO_3 | 220 | 0.56 | 392 | $5.1 \times 10^{-2}$ | 100 | - | 10 |
| $TiO_2$ | 530 | 1.14 | 462 | $6.0 \times 10^{-2}$ | 100 | - | 25 |
| Al | 100 | 0.01 | 1000 | $7.6 \times 10^{-2}$ | - | 100 | 15 |

ZnO_1 (table 4.5), the polystyrene slab melted. We believe that this happened because the temperature of the polymer far exceeded the glass transition temperature, $T_g$. According to the literature, the value for $T_g$ is around 100°C [71]. Considering the power applied at the terminals and the time of the deposition, it is very likely that the polymer was in the transient phase. In figure 4.10 it is possible to confirm how highly deformed the slab was. It is worth mentioning that the PMMA slab was left intact and made it through the deposition process.

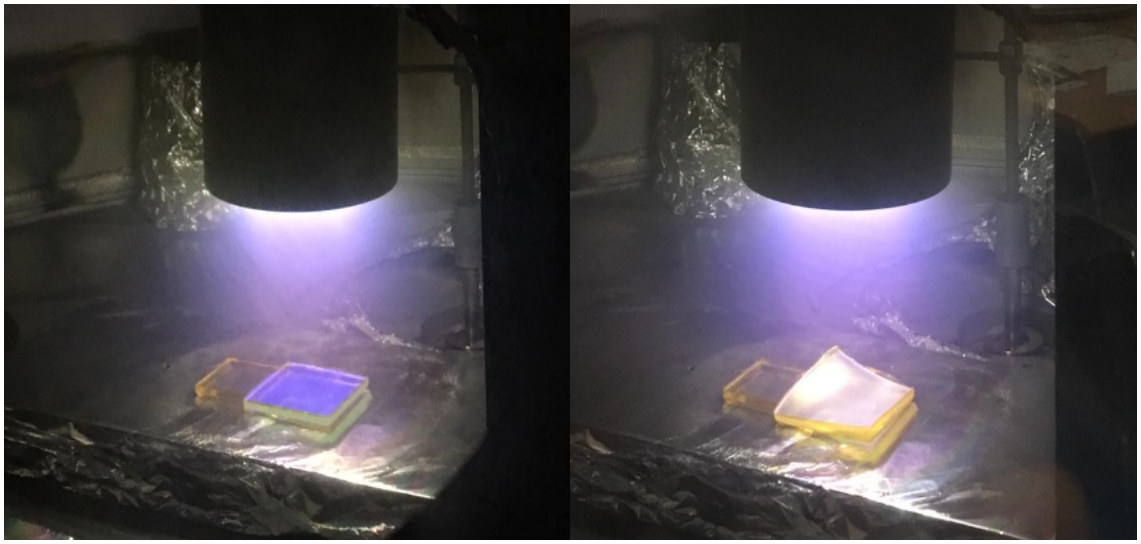

(a) Substracts during the film deposition. (b) Substracts after the film deposition.

Figure 4.10: Photograph of the experimental setup for the magnetron sputtering technique. On the left there is a PMMA slab, on the right, and centered with the electrodes, a Polystyrene slab.

With the previous result in consideration, the following depositions were done with a lower power and with a time of deposition of 10 minutes. These parameters proved to be more adequate as the phenomenon mentioned previously did not occur for these conditions. It is expected that the film from ZnO_3 is thicker than the one in ZnO_2, as the power was lower for the latter.

As far as $TiO_2$ is concerned, the optimal parameters were known, as several studies had been done previously with the same system [66], therefore only one deposition was done. There was also one attempt of using this technique to deposit aluminium onto the substracts. However, the system was very unstable and lead to the aluminium being burn

and not depositing uniformly over the substract.

#### 4.4.1.1 Spectrophotometry

A spectrophotometer was used to analyse the transmittance of the films in respect to the different conditions and coatings. The curves were obtained given that the face with the coating was the first one to interact with the beam.

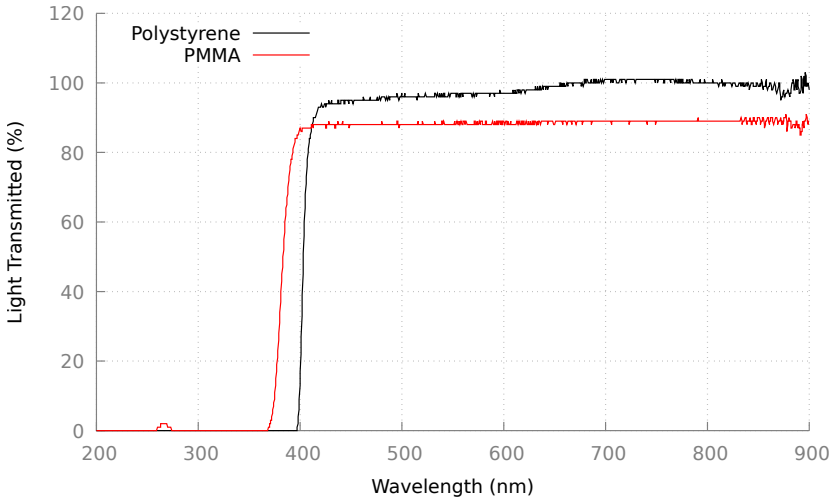


Figure 4.11: Transmittance curves of PMMA and PS slabs.

in figure 4.11 the transmittance curves for PMMA and PS are plotted together. In this figure it is easy to verify that PS has an overall higher transmittance coefficient than PMMA. This result is coherent with one of the functionalities of the optical fibres' cladding which is to increase the light trap efficiency. Another interesting observation is that the PS curve drops earlier, for a wavelength of 400 nm, whereas PMMA drops only at 370 nm.

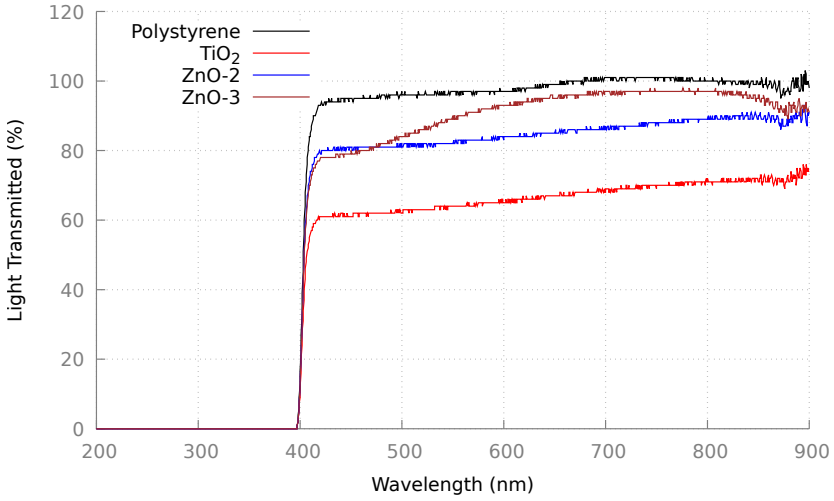


Figure 4.12: Transmittance curves for PS slabs in different conditions.

As for figure 4.12 it suggests that $TiO_2$ might be the most adequate coating for PS as it has the lowest transmittance percentage in comparison to the others. Between ZnO-2 and ZnO-3 there is no significant difference, since for 450 nm, which is the peak of absorbance for the scintillating fibres both show about the same result. The fact that ZnO-3 curve has a maximum probably has to do with the impurities trapped during depositions and the scratches that the samples had prior to this work.

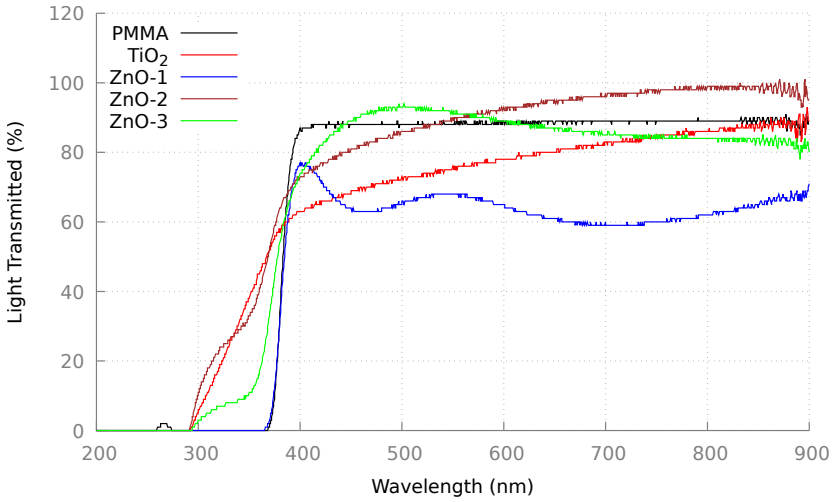


Figure 4.13: Transmittance curves for PMMA slabs in different conditions.

In all the curves there is a small turbulence near high wavelength values, probably related with the equipment limitations. The reason for this was that the acquisitions were done in fast mode. An easy way to mitigate this effect would be to use a slower acquisition mode.

Finally, for figure 4.13, the curves behave differently from what was observed in the previously. For these curves there are significant oscillations in the percentage of light transmitted. It is our understanding that the main reason for this is the nonuniformity in the thickness of the film. This is especially relevant because of how the slabs were placed underneath the cathode, as explained in section 4.4.1. This variation in the film thickness also affects how the curves drop, resulting in some cases in a slower decline until values of 0% of transmittance. Looking once again solely at the transmittance rate, the films that seem more adequate are Ti$O_2$ and ZnO_1, which although do not intersect at 450 nm, if the film thickness was uniform over the subtract, we would possibly get a more conclusive result.

### 4.4.2 Thermal Evaporation

In this work, thermal evaporation technique was only used to deposit the aluminium films onto the substrates and scintillating fibre. To do the deposition, small segments of an aluminium thread were cut and placed in the tungsten resistance. This thread was

highly pure (99,5%) in aluminium [64]. The conditions for each deposition can be found in table 4.6. Each deposition lasted 1 minute.

Table 4.6: Pressure, current and voltage parameters to deposit aluminium using thermal evaporation.

| | Pressure (mbar) | Current (A) | Voltage (V) |
|---|---|---|---|
| 1 | $4.5 \times 10^{-5}$ | 40 | 4 |
| 2 | $3.0 \times 10^{-5}$ | 51 | 5 |
| 3 | $2.8 \times 10^{-5}$ | 48 | 4 |

The results obtained from thermal evaporation were very positive, not only the deposition was much faster than those using magnetron sputtering technique, as we obtained a much clearer aluminium reflective mirror. Aluminium was also deposited on a small fibre segment (3) and the result was also very positive, although the mirror can break if the optical fibre is subjected to significant deformations such as bending.

#### 4.4.2.1 Adherence Test

After applying the aluminium coating to all the test slabs their adherence to the middle coating was tested by using a Tesa transparent film tape. In order to have the same testing conditions it was decided that the same person would do all the testing and all at once, the person in question should try to pull the tape always in the same angle, the tape would always be applied to the centre of the slab.

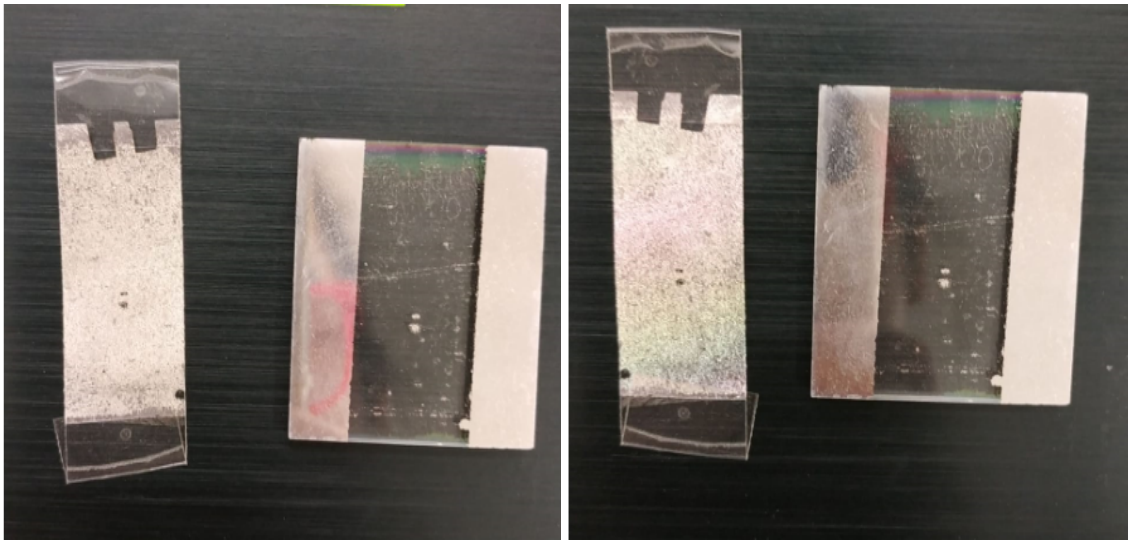

(a) Tape and substract after adherence test for ZnO_3.

(b) Tape and substract after adherence test for ZnO_1.

Figure 4.14: Photographs of the tape used to remove the aluminium coating for different depositions.

This test revealed to be inconclusive since all the films came out in only one pull. In the ZnO_1 PMMA slab the tape also took a significant amount of the intermediate coating

besides the aluminium. These results does not say much in regard to the increase of the adherence by using an intermediate coating between the slab and the aluminium.

### 4.4.3 Depositions Discussion

Considering the results obtained previously about the film deposits there could be two possible way to consider the results obtained:

1. Considering the intermediate coating solely as a glue agent - For this evaluation the most important aspect to analyse is the results obtained in section 4.4.2.1. Even though the results were not significant to reach a definite conclusion, what can be said is that studying conditions between ZnO_1 and ZnO_3 might be worthwhile. ZnO_3 did not deform the substracts but the adhesion test did not pull visible amounts of intermediate coating. Depositing $TiO_2$ with higher power might also prove to have similar results to ZnO_1.

2. Considering the intermediate coating not only as a glue agent, but also an extra cladding to further increasing light trapping - In this case, the transmittance percentage has more weight than the adherence to the aluminium. Taking into consideration what was said in section 4.4.1.1, $TiO_2$ is the coating that presumably presents better results for light trapping.

Given that each analysis suggests a different coating, it is our understanding that further work needs to be done with these films to reach a verdict.

## 4.5 Simulations of the Optical Fibre Response

FLUKA was used to study how the optical fibres would behave as a beam profile monitor and high-resolution dosimeter in a radiotherapy setup. The rationale was to start by a simple setup, and once the results went accordingly with what was expected, add extra layers of complexity to the scripts. All results presented were calculated with statistics of $10^9$ protons.

For the first set of simulations we wanted to validate the position of each Bragg peak for different energies. To do so, 5 files were created where a rectangular proton beam was depositing all its energy inside a water target located at $z = 100$ cm and 50 cm long, surrounded by a void sphere for sake of simplicity. The only parameter that changed in this first setup was the energy, thus 250, 200, 150, 100 and 50 MeV beams were studied separately since typical energies for proton therapy ranges from 70 MeV up to 250 MeV [6, 26]. When we look at figure 4.16 with figure 2.3 it is possible to see that there are accentuate ripples between each simulation. This would be easily fixed by increasing the number of simulations, for instance, instead of 5, using 10, with shorter energy gaps.

In the second set of simulations instead of adjusting the beam's energy, we introduced a lucite slab in the system, increasing its thickness to weaken the beam's energy and

therefore mimic a range modulator as described in section 2.5.1. An air sphere was also introduced involving the system and contained inside the void sphere. It is expected that this air sphere increases, although not significantly, the beam's aperture.

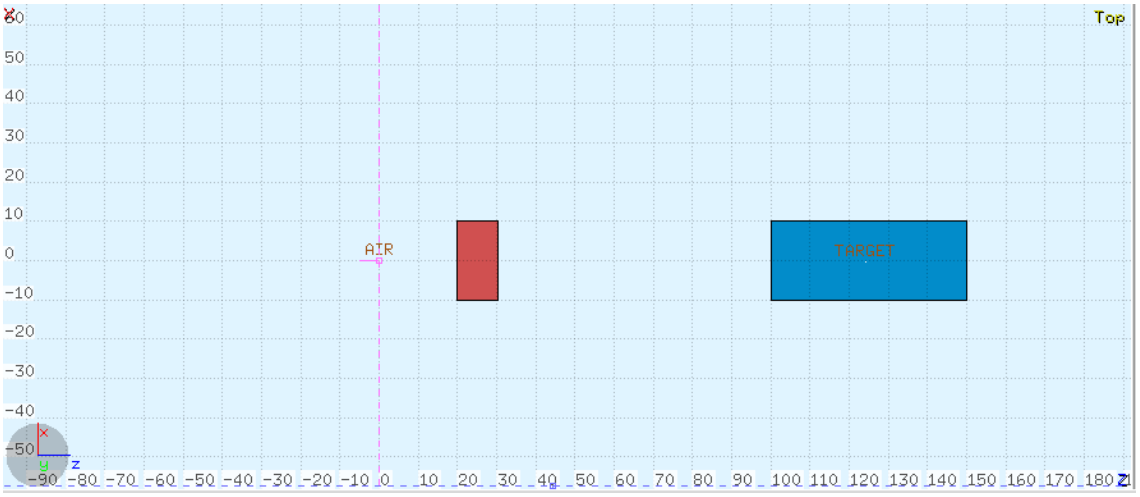


Figure 4.15: Schematic representation of the setup in a second version of the Monte Carlo simulation for a beam of 250 MeV reduced to 200 MeV by a lucite range modulator.

To determine the thickness of the lucite to have our beam decrease from an energy $E_0$ to an energy $E_1$ we should determine what the CSDA range is for each energy (i.e. consulting NIST database) for lucite, subtract the range values and then use devide by the density to determine the thickness for each energy.

As for the third and last setup, we wanted to see how well the 250 $\mu$m fibres would do in determining the dose deposition perpendicularly to the beam. Here, it was decided that the energy studied would be of 200 MeV. The reason for this is if we chose 250 MeV there would be no lucite and 200 MeV is the second highest energy studied so far, possibly making the results interpretation easier. Four points of the dose curve were chosen to study the transverse deposition, $z = 105, 124, 125$ and 126. In figure 4.17 it is possible to see a section of the geometry where the optical fibres are inside the body of water. To collect dose deposition data two USRBIN cards were created, one where we had bins of 0.2×0.2×0.5 mm (x, y, z), and another which would collect data by individual region, in this case, 800 polystyrene cylinders mimicking the optical fibres.

The data collected from the dose of the polystyrene cylinders (fibres) had energy depositions considerably lower than the data collected in the water. To correctly compare both plots we normalized the data from fibres by multiplying every point of the file by the quotient of the max of the binning by the max of the region file. The reason why these dose values are 2 orders of magnitude apart is because the USRBIN for "water", are considering volumetrically larger voxels than for the points in orange as "fibres". While water has voxels of 500 $\mu m^3$, the region simulation, or fibres, only accounts for the volume of the cylinder which is 98 $\mu m^3$, making the first volume almost 5 times bigger than the latter and therefore adding up to a higher total dose for each point.

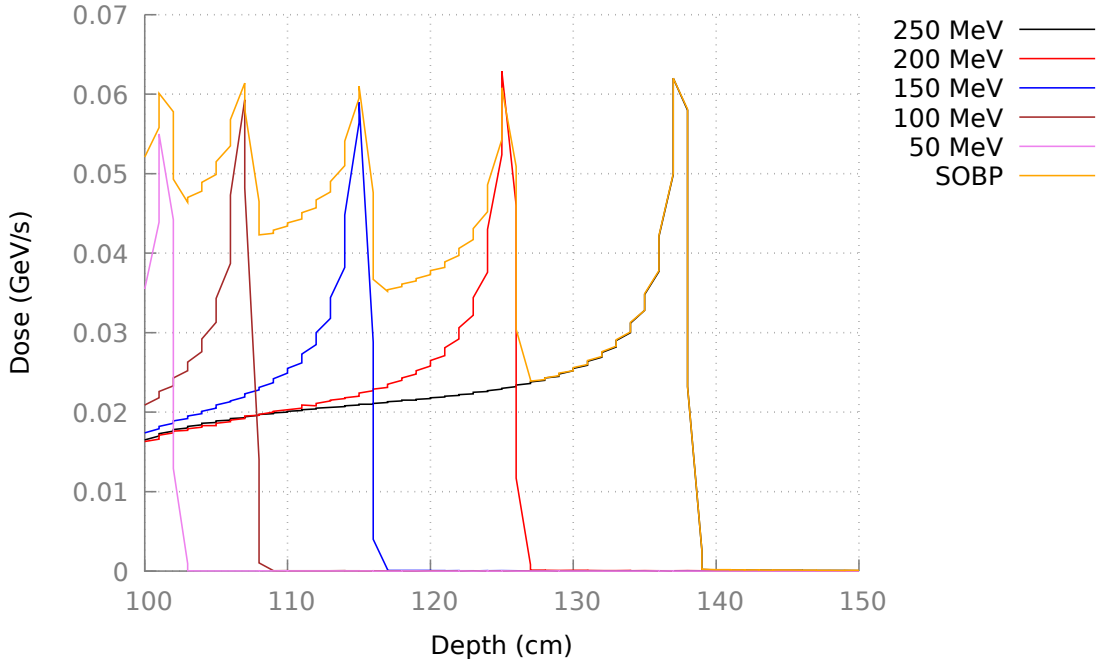


Figure 4.16: Spread out Bragg peak simulated in a body of water with beams of energies 250, 200, 150, 100 and 50 MeV. A slab of lucite was added to the system to reduce the beam's energy.

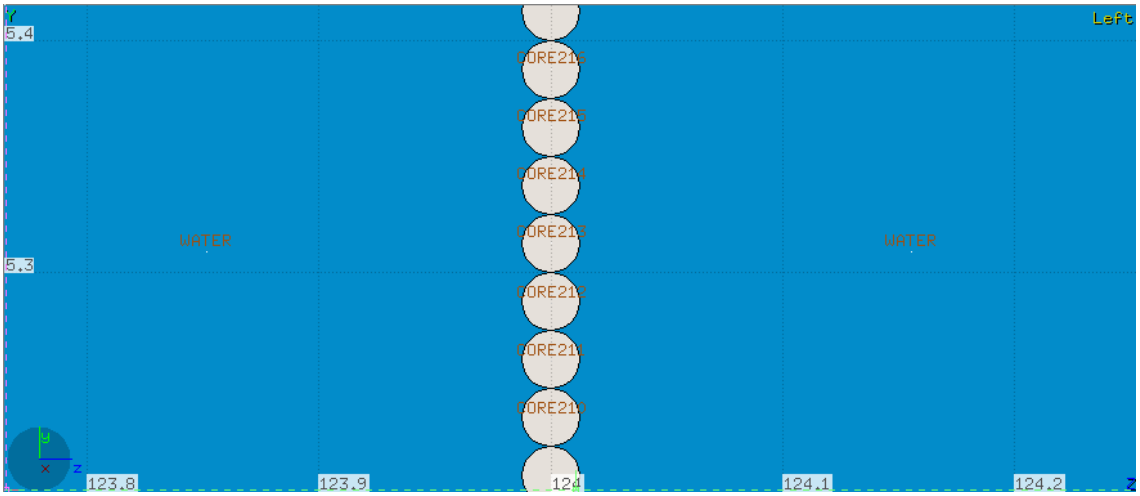


Figure 4.17: Schematic representation of the optical fibres inside the water target on a version of the Monte Carlo simulation for a beam of 250 MeV reduced to 200 MeV by a lucite range modulator.

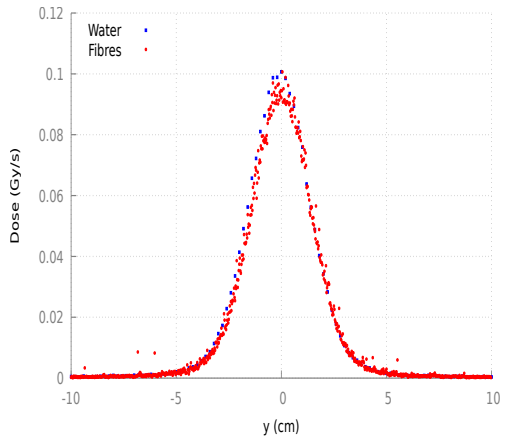


a Graphical representation of the transverse dose deposited at z = 105 cm.

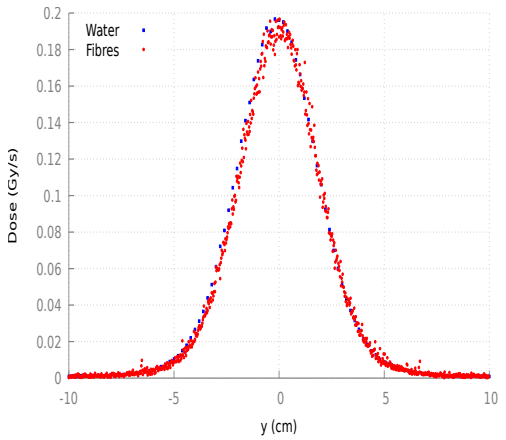


b Graphical representation of the transverse dose deposited at z = 124 cm.

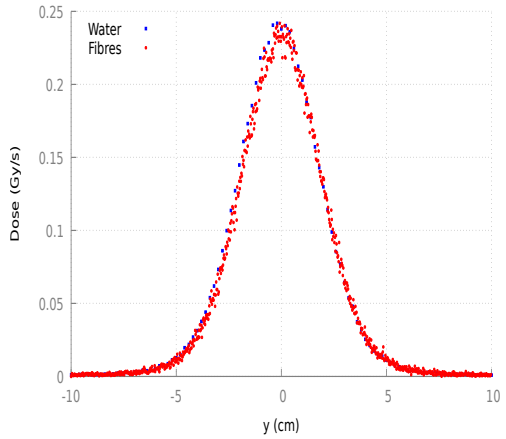


c Graphical representation of the transverse dose deposited at z = 125 cm.

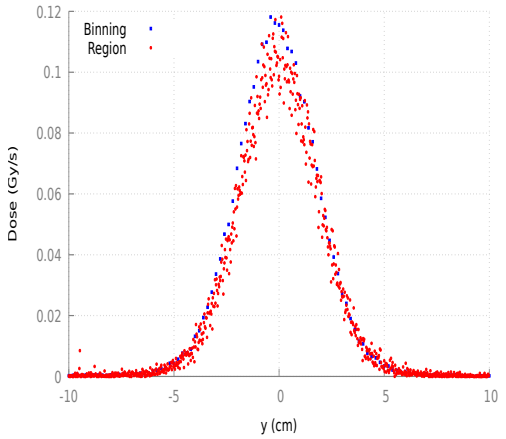


d Graphical representation of the transverse dose deposited at z = 126 cm.

Figure 4.18: Set of graphs of the transverse dose profile for 200 MeV in the third simulation setup.

Taking a closer look at each graph in figure 4.18, in figure 4.18a the dose peaks for a value of almost 0.12 Gy/s. For figure 4.18b, which corresponds to the build up region of the Bragg peak. Here we can observe a rise in the maximal transverse dose as well as a widening of the beam. As for figure 4.18c, which corresponds to the Bragg peak, we have the maximum dose which accounts for 0.25 Gy/s. Finally, in figure 4.18d we have the transverse dose corresponding to the Bragg peak drop, even having an abrupt lowering of the dose maximum. Here we can observe that there is a significant amount of dispersion.

In fact, if we look at figures 4.19 and 4.20, which were plotted using data from USRBIN cartesian, for a step in x and y of 0.2 mm from the origin the map remains the same colour. Looking at the transverse dose deposition by region gives us a higher sense of granularity, than with a resolution of 500 $\mu$m. This might explain why in all of the sub figures in figure 4.18 the peaks never match except for figure 4.18b where we have the maximum

dose deposition. Figure 4.18d shows that the dose deposition decreases quickly after the Bragg peak.

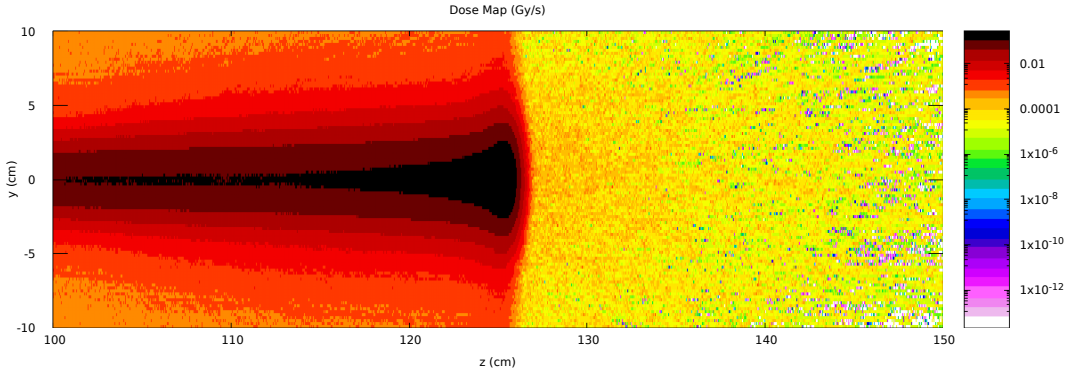


Figure 4.19: Distribution of the energy deposition for the third setup along the yOz plane.

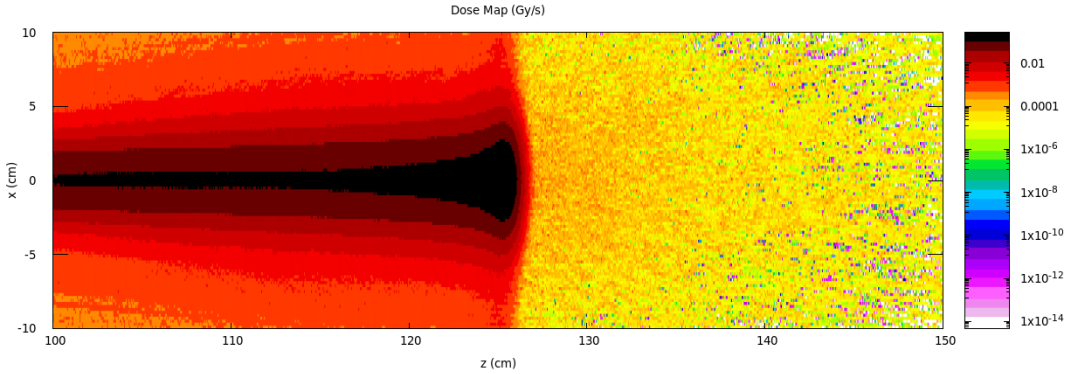


Figure 4.20: Distribution of the energy deposition for the third setup along the xOz plane.

Chapter 5

# Conclusions

## 5.1 Overview

While radiotherapy has emerged as an innovative way to treat multiple types of cancer, there is a huge demand for devices which can quickly profile the beam with as much resolution as possible both spatially and temporally. Even though there are already dosimeters with high resolution (like TEPC and novel Si-dosimeters), they have certain drawbacks. The TEPC requires operating at high voltages and a gas assembly system. Si-dosimeters still need to overcome problems with recombination effects that can limit the charge collection efficiency, poor signal-to-noise ratio, energy dependent conversion to tissue-equivalent doses, and radiation deterioration. Scintillating fibres cannot, in principle, reach micrometer resolutions and are affected by the quenching effect, but have the advantage of being cheap, having a reasonable sub millimetric resolution and being tissue equivalent. As explained in section 1.1, these detectors allows us to measure radiation which has a wide range of applications for both radiation medicine as well as radiation protection.

There is still little work done using scintillating fibres as a detector material, both for therapeutic purposes and space protection. In space, one of the principal concerns when assembling a detector device is the necessity to have robust materials which can withstand radiation for long periods of time without losing much of its physical characteristics. In this way, this study is the beginning of a project that will be continued in the next years in which the ultimate goal is to develop a sub millimetric dosimeter using scintillating fibres to be used in radiotherapy and space studies.

## 5.2 Summary and Future Work

Considering the results obtained for the film deposits, it might be interesting to continue exploring different parameters for ZnO since it showed better adherence to the aluminium than $TiO_2$. In this regard it should be kept in mind that the geometry of the substract used was quadrangular and that our optical fibres are circular. Once again, this compels us to encourage to continue these studies also using quadrangular optical fibres or explore other kind of optical fibres such as 3HF, another kind of scintillating fibres, as suggested by the Heidelberg group. Concerning thermal evaporation, the aluminium deposits were very good, both for the substracts as well as for the fibre, although showed poor adherence to the substracts. Because LIP has focused mostly on depositions using magnetron sputtering, trying to use thermal evaporation to do all the aluminium deposits might bring some new perspectives. Not to mention that the process is a lot quicker than magnetron sputtering. Another interesting aspect to explore is whether or not it is viable to configure our magnetron system so that we can rotate the fibres during sputtering deposition, as well as being able to accommodate fibres of up to two meters. For this it would be necessary to design specific components as well as a control system that would allow us to move the fibres from outside the system.

In this work we successfully designed and produced a tray that allows to further investigate the plastic fibres' properties, namely the crosstalk effect. The results obtained with this tray will have an enormous impact in the design of the detector prototype. Nevertheless, before we can grasp any crosstalk effect quantification there is still a lot of work ahead in regard to stabilize the system. One of the advantages which was not mentioned previously is that With this tray it is possible to illuminate each different fibre diameter at the same distance from the LED, which was not possible for the old setup.

The next step in the Monte Carlo simulations is to add the PMMA coating surrounding the PS cylinders and check if there is any difference in the results. Simulations could also be further developed by including the subsequent optical photon propagation in the optical fibres allowing the characterization of the system response to different irradiation conditions. A different simulation should be done to evaluate the crosstalk effect expected behaviour, helping with the stabilization of the system as well as trying to estimate the quantity of Cerenkov radiation produced.

To characterize the scintillating fibres under proton irradiation it is necessary to access an accelerator facility. Although the installation of a proton therapy installation in Portugal is foreseen for the next years, it is possible to already make some assessments with a very low energy (~2 MeV) proton microbeam at the CTN, Lisbon, or with the 18 MeV beam at the ICNAS cyclotron, Coimbra. Those responsible for these facilities showed willingness to cooperate in our experiments, but there was no availability during the period of this thesis. The goal with these measurements would be to determine the light yield as a function of the proton stopping power and to obtain the scintillating fibres' efficiency and Birks' constant. These parameters once incorporated into the simulations

would give more realistic results, namely quantifying the quenching effect on a scintillating fibre array. To perform these measurements it would be necessary to design a new support system adapted to the irradiation conditions. This support should also be able to measure crosstalk effects during proton radiation.

# Bibliography


[1] F. H. Attix. *Introduction to Radiological Physics and Radiation Dosimetry*. Wiley-VCH, 1986. ISBN: 978-0-471-01146-0.

[2] J. Cameron. "Radiation dosimetry." In: *Environmental health perspectives* 91 (1991), 45–48. DOI: 10.1289/ehp.919145.

[3] M. Bardies and P. Pihet. "Dosimetry and microdosimetry of targeted radiotherapy." In: *Curr. Pharm. Des.* 6.14 (Sept. 2000), pp. 1469–1502. DOI: 10.2174/1381612003399176.

[4] S. Gianfaldoni, R. Gianfaldoni, U. Wollina, J. Lotti, G. Tchernev, and T. Lotti. "An Overview on Radiotherapy: From Its History to Its Current Applications in Dermatology." In: *Open access Macedonian journal of medical sciences* (2017), 521–525. DOI: 10.3889/oamjms.2017.122.

[5] P. P. Connell and S. Hellman. "Advances in Radiotherapy and Implications for the Next Century: A Historical Perspective." In: *Cancer Res.* 69.2 (2009), pp. 383–392. DOI: 10.1158/0008-5472.CAN-07-6871.

[6] W. Newhauser and R. Zhang. "The physics of proton therapy." In: *Phys. Med. Bio.* 60 (Mar. 2015), R155–R209. DOI: 10.1088/0031-9155/60/8/R155.

[7] H. Giap and B. Giap. "Historical perspective and evolution of charged particle beam therapy." In: *Transl Cancer Res* 1.3 (2012), pp. 127–136. DOI: 10.3978/j.issn.2218-676X.2012.10.09.

[8] H. H. Rossi and M. Zaider. *Microdosimetry and Its Applications*. Springer, 1996. DOI: 10.1007/978-3-642-85184-1.

[9] C. M. Washington and D. T. Leaver. *Principles and Practice of Radiation Therapy*. Fourth. Elsevier. ISBN: 007-124476-X.

[10] M. W. Charles. "ICRP Publication 103: Recommendations of the ICRP." In: *Radiat. Prot. Dosim.* 129.4 (May 2008), pp. 500–507. DOI: 10.1093/rpd/ncn187.

[11] C. Fleta, S. Esteban, M. Baselga, D. Quirion, G. Pellegrini, C. Guardiola, M. Cortés-Giraldo, J. G. López, M. J. Ramos, F. Gómez, and M. Lozano. "3D cylindrical silicon microdosimeters: fabrication, simulation and charge collection study." In: *J. Instrum.* 10.10 (Oct. 2015). DOI: 10.1088/1748-0221/10/10/p10001.

[12] G. A. Santa Cruz. "Microdosimetry: Principles and applications." In: *Rep. Pract. Oncol. Radiother.* 21.2 (2016), pp. 135–139. DOI: 10.1016/j.rpor.2014.10.006.

[13] T. Sato, R. Watanabe, and K. Niita. "Development of a calculation method for estimating specific energy distribution in complex radiation fields." In: *Radiat. Prot. Dosi.* 122.1-4 (Nov. 2006), pp. 41–45. DOI: 10.1093/rpd/nc1407.

[14] A. B. Rosenfeld. "Novel detectors for silicon based microdosimetry, their concepts and applications." In: *Nucl. Instrum. Methods Phys. Res., Sect. A* 809 (2016), pp. 156 –170. DOI: https://doi.org/10.1016/j.nima.2015.08.059.

[15] R. Grun, T. Friedrich, M. Kramer, K. Zink, M. Durante, R. Engenhart-Cabillic, and M. Scholz. "Physical and biological factors determining the effective proton range." In: *Med. Phys.* 40.11 (Nov. 2013).

[16] M. Niemantsverdriet, M.-J. van Goethem, R. Bron, W. Hogewerf, S. Brandenburg, J. A. Langendijk, P. van Luijk, and R. P. Coppes. "High and Low LET Radiation Differentially Induce Normal Tissue Damage Signals." In: *Int. J. Radiat. Oncol.* 83.4 (2012), pp. 1291 –1297. DOI: https://doi.org/10.1016/j.ijrobp.2011.09.057.

[17] M. Howard, C. Beltran, J. Sarkaria, and M. G. Herman. "Characterization of relative biological effectiveness for conventional radiation therapy: a comparison of clinical 6 MV X-rays and 137Cs." In: *J. Radiat. Res.* 58.5 (Sept. 2017), pp. 608–613. DOI: 10.1093/jrr/rrx018.

[18] G. Barendsen. "RESPONSES OF CULTURED CELLS, TUMOURS, AND NORMAL TISSUES TO RADIATIONS OF DIFFERENT LINEAR ENERGY TRANSFER." In: *pp 293-356 of Current Topics in Radiation Research. Vol. IV. Ebert, Michael Howard, Alma (eds.). New York, John Wiley and Sons, Inc., 1968.* (Oct. 1968).

[19] J. J. P. Lima. *Física em Medicina Nuclear*. Imprensa da Universidade de Coimbra, 2008. ISBN: 9789898074263.

[20] H. Paganetti. *Proton Therapy Physics*. CRC Press, 2012. ISBN: 978-1-4398-3645-3.

[21] G. W. Barendsen. "The Relationships between RBE and LET for Different Types of Lethal Damage in Mammalian Cells: Biophysical and Molecular Mechanisms." In: *Int. J. Radiat. Res.* 139.3 (1994), pp. 257–270. DOI: 10.2307/3578823.

[22] K. K. Fu, T. L. Phillips, D. C. Heilbron, G. Ross, and L. J. Kane. "Relative biological effectiveness of low- and high-LET radiotherapy beams for jejunal crypt cell survival at low doses per fraction." In: 132.1 (July 1979), pp. 205–209. DOI: 10.1093/jrr/rrx018.

[23] H. Paganetti, A. Niemierko, M. Ancukiewicz, L. E. Gerweck, M. Goitein, J. S. Loeffler, and H. D. Suit. "Relative biological effectiveness (RBE) values for proton beam therapy." In: *Int. J. Radiat. Oncol.* 53.2 (2002), pp. 407 –421. DOI: https://doi.org/10.1016/S0360-3016(02)02754-2.

[24] H. Nikjoo, R. J. Munson, and B. A. Bridges. "RBE-LET relationships in mutagenesis by ionizing radiation." In: *J. Radiat. Res.* 40 Suppl (Dec. 1999), pp. 85–105.

[25] T. Takatsuji, I. Yoshikawa, and M. S. Sasaki. "Generalized concept of the LET-RBE relationship of radiation-induced chromosome aberration and cell death." In: *J Radiat Res.* (Mar. 1999). DOI: 10.1269/jrr.40.59.

[26] C.-J. Tung. "Microdosimetric relative biological effectiveness of therapeutic proton beams." In: *Biomed. J.* 38 5 (2015), pp. 399–407. DOI: 10.4103/2319âĂŚ4170.167072.

[27] National Institute of Health. *Radiation Therapy to Treat Cancer*. May 13, 2019. 2018. URL: https://www.cancer.gov/about-cancer.

[28] J. Berger, J. Coursey, M. Zucker, and J. Chang. *Stopping powers and ranges for protons and alpha particles*. May 13, 2019. 2017. URL: https://physics.nist.gov/PhysRefData/Star/Text/ASTAR.html.

[29] J. Berger, J. Coursey, M. Zucker, and J. Chang. *ESTAR, PSTAR, and ASTAR: Computer Programs for Calculating Stopping-Power and Range Tables for Electrons, Protons, and Helium Ions (version 2.0.0)*. May 13, 2019. 2005. URL: https://physics.nist.gov/PhysRefData/Star/Text/PSTAR.html.

[30] D. Jette and W. Chen. "Creating a spread-out Bragg peak in proton beams." In: *Phys. Med. Bio.* 56 (June 2011), N131–8. DOI: 10.1088/0031-9155/56/11/N01.

[31] H. Paganetti and T. Bortfeld. "Proton Beam Radiotherapy - The State of the Art1." In: *Med. Phys.* 32 (Jan. 2005).

[32] B. Dunbar. *Why Space Radiation Matters*. September 21, 2019. 2018. URL: https://www.nasa.gov/analogs/nsrl/why-space-radiation-matters.

[33] S. Frazier. *Real Martians: How to Protect Astronauts from Space Radiation on Mars*. September 21, 2019. 2015. URL: https://www.nasa.gov/feature/goddard/real-martians-how-to-protect-astronauts-from-space-radiation-on-mars.

[34] Health Physics Society. *Radiation Exposure During Commercial Airline Flights*. October 06, 2019. 2016. URL: https://hps.org/publicinformation/ate/faqs/commercialflights.html.

[35] J. Madigan. *About RaD-X*. October 03, 2019. 2019. URL: https://science.larc.nasa.gov/radx/about-instruments.html.

[36] S. Beddar and L. Beaulieu. *Scintillation Dosimetry*. CRC Press, 2016. ISBN: 9781482208993.

[37] J. L. Hoff and L. W. Townsend. "MCNP Modelling of the Wall Effects Observed in Tissue-equivalent Proportional Counters." In: *Radiat. Prot. Dosim.* 99.1-4 (June 2002), pp. 369–370. DOI: 10.1093/oxfordjournals.rpd.a006805.

[38] L. Archambault, J. Arsenault, L. Gingras, A. Sam Beddar, R. Roy, and L. Beaulieu. "Plastic scintillation dosimetry: Optimal selection of scintillating fibers and scintillators." In: *Med. Phys.* 32.7Part1 (June 2005), pp. 2271–2278. DOI: 10.1118/1.1943807.

[39] T. Henry, D. Robertson, F. Therriault-Proulx, and S. Beddar. "Determination of the Range and Spread-Out Bragg Peak Width of Proton Beams Using a Large-Volume Liquid Scintillator." In: *Int. J. Part. Ther* 4.1 (2017), pp. 1–6. DOI: 10.14338/IJPT-17-00001.1.

[40] D. Leverington, M. Dziewiecki, L. Renner, and R. Runze. "A Scintillating Fibre Beam Profile Monitor for Ion Therapy Beams." In: *J. Instrum.* 13 (Dec. 2017). DOI: 10.1088/1748-0221/13/05/P05030.

[41] PhysicsOpenLab. *X Ray Proportional Counter*. April 18, 2019. URL: http://physicsopenlab.org/2017/07/23/x-ray-proportional-counter-2/.

[42] L. W. Brackenbush. *Using Tissue Equivalent Proportional Counters to Determine Dose Equivalent*. Tech. rep. 25014731. U.S. Department of Energy, 1991.

[43] M. Victor and J. Escobedo. *Tissue Equivalent Proportional Counter (TEPC)*. January 27, 2019. URL: https://www.nasa.gov/mission_pages/station/research/experiments/630.html.

[44] Oak Ridge Associated Universities. *Proportional Counters*. January 27, 2019. URL: https://www.orau.org/ptp/collection/proportional\%20counters/introprops.htm.

[45] W. J. Yoo, D. Jeon, J. K. Seo, S. H. Shin, K.-T. Han, W. S. Youn, S. Cho, and B. Lee. "Development of a scintillating fiber-optic dosimeter for measuring the entrance surface dose in diagnostic radiology." In: *Radiat. Meas.* 48 (2013), pp. 29 –34. DOI: https://doi.org/10.1016/j.radmeas.2012.11.001.

[46] K. C. S. Adel S. Sedra. *Microelectronic Circuits*. 6th ed. The Oxford Series in Electrical and Computer Engineering. Oxford University Press, USA, 2009. ISBN: 0195323033,9780195323030.

[47] M.-C. Lavallée, L Gingras, and L. Beaulieu. "Energy and integrated dose dependence of MOSFET dosimeter sensitivity for irradiation energies between 30 kV and 60Co." In: *Med. Phys.* 33 (Nov. 2006), pp. 3683–3689. DOI: 10.1118/1.2349301.

[48] T. Bretz, R. Engel, T. Hebbeker, J. Kemp, L. Middendorf, C. Peters, J. Schumacher, R. Šmída, and D. Veberič. "An integrated general purpose SiPM based optical module with a high dynamic range." In: *J. Instrum.* 13.06 (June 2018). DOI: 10.1088/1748-0221/13/06/p06001.

[49] P. Eraerds, M. Legré, A. Rochas, H. Zbinden, and N. Gisin. "SiPM for fast Photon-Counting and Multiphoton Detection." In: *Opt. Express* 15.22 (Oct. 2007), pp. 14539–14549. DOI: 10.1364/OE.15.014539.

[50] S. Seifert, H. van Dam, J. Huizenga, R. Vinke, P. Dendooven, H. Lohner, and D. R. Schaart. "Simulation of Silicon Photomultiplier Signals." In: *IEEE T. Nucl. Sci.* (Dec. 2009). DOI: 10.1109/TNS.2009.2030728.

[51] T. Kirn. "SciFi – A large scintillating fibre tracker for LHCb." In: *Nucl. Instrum. Methods Phys. Res., Sect. A* 845 (Oct. 2017). Proceedings of the Vienna Conference on Instrumentation 2016, pp. 481 –485. DOI: https://doi.org/10.1016/j.nima.2016.06.057.

[52] S. Girard, D. Francesca, A. Morana, and C. Hoehr. "X-rays, $\gamma$-rays and Proton Beam Monitoring with Multimode Nitrogen-doped Optical Fiber." In: *IEEE T. Nucl. Sci.* PP (Nov. 2018), pp. 1–1. DOI: 10.1109/TNS.2018.2879791.

[53] Kuraray. *Plastic Scintillating Fibers*. Kuraray's booklet on different type of fibers that they commercialize.

[54] C. Kim, B. Hong, G. Jhang, E. Joo, K. S. Lee, S. K. Park, H. H. Shim, S. S. Shin, and K. S. Sim. "Measurement of scintillation responses of scintillation fibers for dose verification in proton therapy." In: *J. Korean Phys. Soc.* 60.5 (Mar. 2012), pp. 725–730. DOI: 10.3938/jkps.60.725.

[55] A. Hibbs. *What is Fluorescence? In: Confocal Microscopy for Biologists*. Springer, 2004. ISBN: 978-0-306-48565-7.

[56] P. McIntyre. "Cross talk in absorbing optical fibers." In: 65.7 (July 1975), pp. 810–813. DOI: 10.1364/JOSA.65.000810.

[57] K. Vo. *Spectrophotometry*. August 6, 2019. 2019. URL: https://bit.ly/2H5YxHn.

[58] M. David, A. Gomes, A. Maio, J. Pina, and B. Tome. "15 years of experience with quality control of WLS flbres for the ATLAS Tile Calorimeter." 2009.

[59] G. S. Bumbrah and R. M. Sharma. "Raman spectroscopy – Basic principle, instrumentation and selected applications for the characterization of drugs of abuse." In: *Egypt. J. Foren. Sci.* 6.3 (2016), pp. 209 –215. DOI: https://doi.org/10.1016/j.ejfs.2015.06.001.

[60] G. Luís. "Efeito de Estimulantes Gustativos de Secreção Salivar na Desmineralização do Esmalte Dentário e Incorporação de Flúor por $\mu$-Raman e PIGE." Master's thesis. Faculdade de Ciências e Tecnologia da Universidade NOVA de Lisboa, Sept. 2017.

[61] P. Vandenabeele. *Pratical Raman Spectroscopy - An Introduction*. Wiley, 2016. ISBN: 978-93-5267-364-3.

[62] S Swann. "Magnetron sputtering." In: *Phys. Technol.* 19.2 (Mar. 1988), pp. 67–75. DOI: 10.1088/0305-4624/19/2/304.

[63] B. Chiad, M. Khalaf, F. Kadhim, and O. Hammadi. "Characteristics and Operation Conditions of a Closed-Field Unbalanced Dual Magnetrons Plasma Sputtering System." In: *Libr. J.* 1 (2014), pp. 1–7. DOI: 10.4236/oalib.1100650.

[64] L. Silva. "Desenvolvimento e caracterização de filmes de nano-compósitos de $TiO_2/WO_3$ pela técnica de pulverização catódica." Master's thesis. Faculdade de Ciências e Tecnologia da Universidade NOVA de Lisboa, Sept. 2012.

[65] P. Mathew, J. George, S. Mathews T, and P J Kurian. "Experimental verification of modified Paschen's law in DC glow discharge argon plasma." In: *AIP Adv.* 9 (Feb. 2019). DOI: 10.1063/1.5086246.

[66] P. Farinha. "Desenvolvimento de dispositivos de conversão e armazenamento de carga utilizando filmes finos de PAZO." Master's thesis. Faculdade de Ciências e Tecnologia da Universidade NOVA de Lisboa, Jan. 2016.

[67] A. F. A. Ferrari P.R. Sala and J. Ranft. *FLUKA: a multi-particle transport code*. last accessed January 24, 2019. 2005. URL: http://www.fluka.org/fluka.php.

[68] T. T. Karthick and P. Tandon. "A short review on the experimental and theoretical aspects of vibrational spectroscopy of polymer." In: (2016), pp. 15–21.

[69] Y. Yang, G. Wu, S. Ramalingam, and S. L. Hsu. "Spectroscopic Analysis of Amorphous Structure in Fluorinated Polymers." In: *Macromolecules* (2007), pp. 9658–9663. DOI: https://doi.org/10.1021/ma071681m.

[70] J. Calles, J. Bermudez, E. Vallés, D. Allemandi, and S. Palma. "Polymers in Ophthalmology." In: Dec. 2015, pp. 147–176. DOI: 10.1007/978-3-319-12478-0_6.

[71] B. Wunderlich. *Thermal Analysis of Polymeric Material*. Springer, July 2005. ISBN: 9783540236290.

ANNEX I

# ANNEX I FIBRES' TRAY

B (1:1)

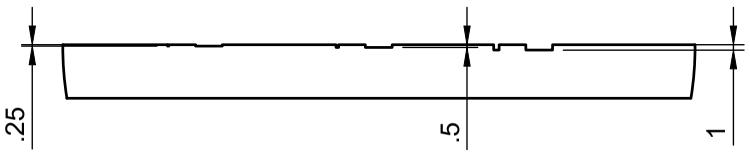


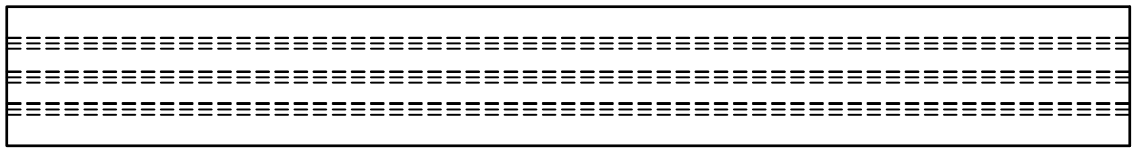

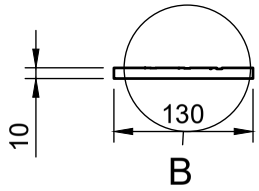


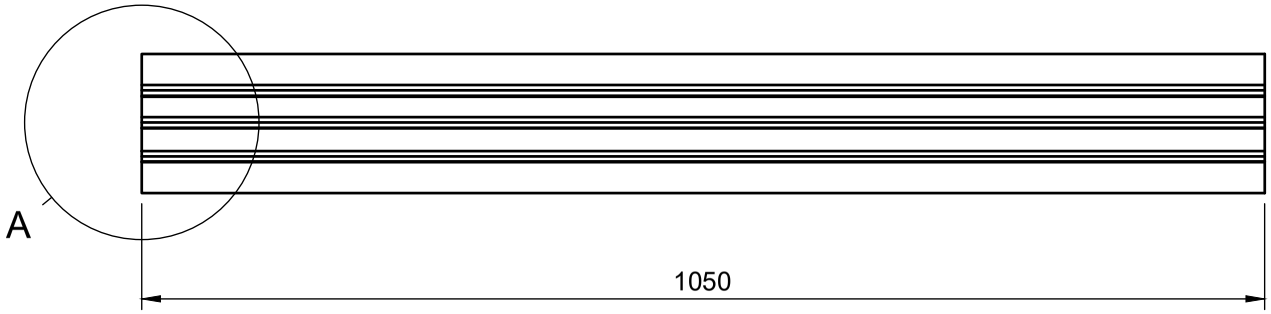


A (1:1.5)

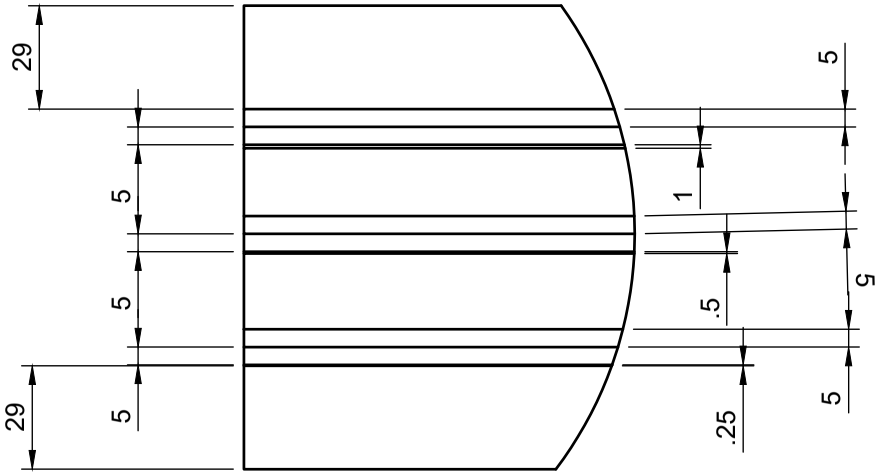


| Dept. | Technical reference | Created by | Approved by |
|---|---|---|---|
| | | Filipa Fragoso 16/09/2019 | |
| | | Document type | Document status |
| | | Title: Suporte_Fibras_Vertical | DWG No. |
| | | | Rev. / Date of issue / Sheet: 1/2 |

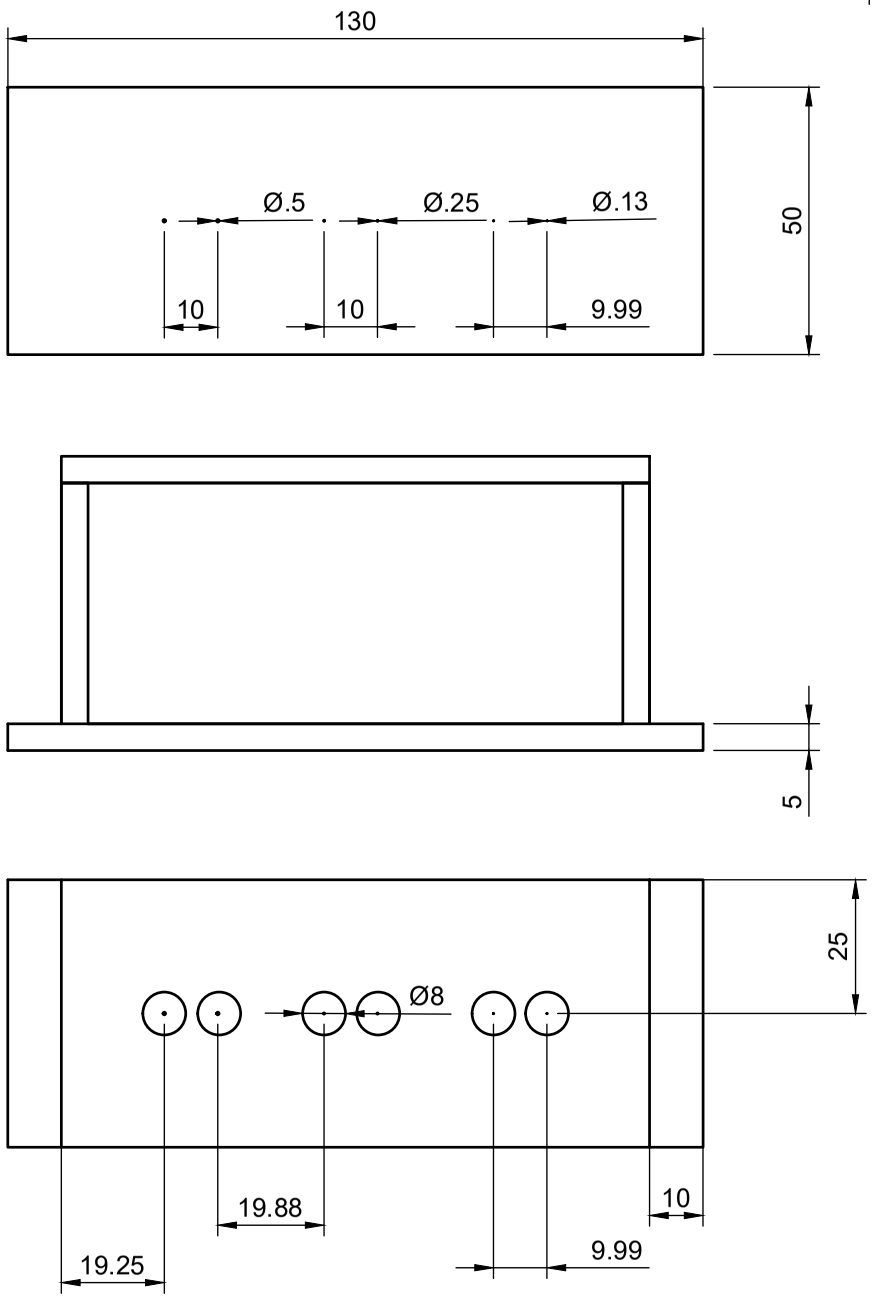


| Dept. | Technical reference | Created by | Approved by |
|---|---|---|---|
| | | Filipa Fragoso 16/09/2019 | |
| | | Document type | Document status |
| | | Title: Suporte_Fibras_Vertical | DWG No. |
| | | | Rev. / Date of issue / Sheet: 2/2 |